Cell Reports
Methods

Article

Tools for efficient analysis of neurons in a 3D reference atlas of whole mouse spinal cord

Graphical abstract

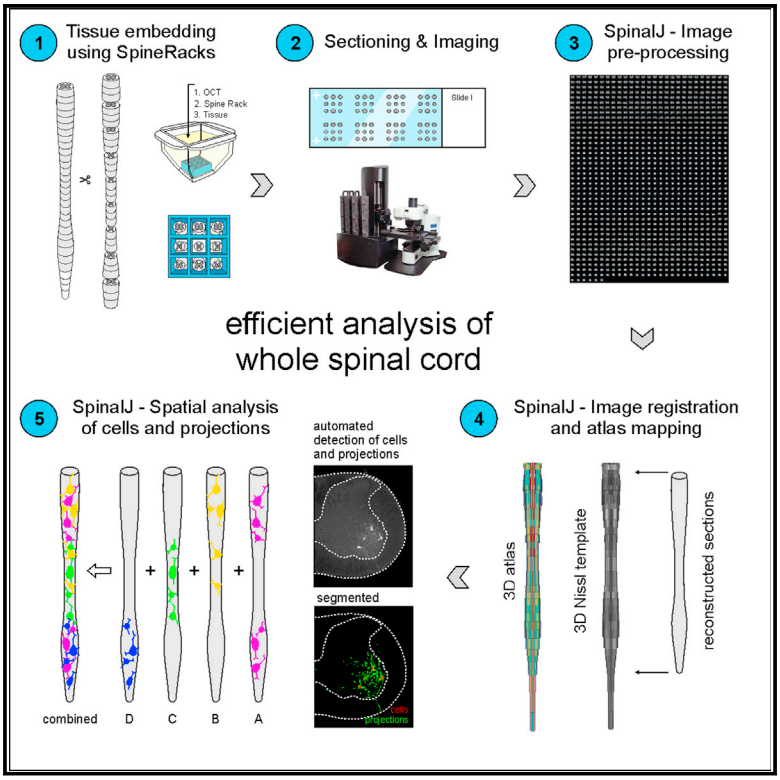

Highlights

- SpineRacks facilitate efficient sectioning and imaging of whole mouse spinal cord
- SpinalJ allows registration, mapping, and analysis of spinal sections
- A 3D atlas provides a common framework for comparative analyses of neurons

Authors

Felix Fiederling, Luke A. Hammond, David Ng, Carol Mason, Jane Dodd

Correspondence

ff2397@columbia.edu (F.F.), jd18@columbia.edu (J.D.)

In brief

Fiederling et al. provide tools for efficient analysis of neurons and their processes within the entire mouse spinal cord. A 3D reference atlas puts images into anatomical context and allows integration of data from different studies. They demonstrate the usefulness of this methodology, analyzing known and previously unknown neuronal distributions.

Fiederling et al., 2021, Cell Reports Methods *1*, 100074
September 27, 2021
https://doi.org/10.1016/j.crmeth.2021.100074

CellPress

Cell Reports Methods

CellPress
OPEN ACCESS

Article

Tools for efficient analysis of neurons in a 3D reference atlas of whole mouse spinal cord

Felix Fiederling,[1,*] Luke A. Hammond,[2] David Ng,[2] Carol Mason,[3] and Jane Dodd[1,4,*]
[1]Departments of Physiology & Cellular Biophysics, and Neuroscience, Zuckerman Institute, Columbia University, New York, NY 10027, USA
[2]Zuckerman Institute, Columbia University, New York, NY 10027, USA
[3]Department of Pathology and Cell Biology, Neuroscience, and Ophthalmology, Zuckerman Institute, Columbia University, New York, NY 10027, USA
[4]Lead contact
*Correspondence: ff2397@columbia.edu (F.F.), jd18@columbia.edu (J.D.)
https://doi.org/10.1016/j.crmeth.2021.100074

MOTIVATION Spinal neurons are highly heterogeneous in location, transcriptional identity, and function. To understand their contributions to sensorimotor circuits, it is essential to map the positions of identified subsets of neurons in relation to others throughout the spinal cord (SC), but we lack tools for whole-SC sample preparation, imaging, and *in toto* analysis. We therefore developed tools to improve sectioning efficiency of whole SC and to enable section registration, atlas mapping, and 3D analysis. These permit, for the first time, SC-wide analysis with high spatial precision and comparison and integration of results from different samples and across research groups.

SUMMARY

To fill the prevailing gap in methodology for whole spinal cord (SC) analysis, we have (1) designed scaffolds (SpineRacks) that facilitate efficient and ordered cryo-sectioning of the entire SC in a single block, (2) constructed a 3D reference atlas of adult mouse SC, and (3) developed software (SpinalJ) to register images of sections and for standardized analysis of cells and projections in atlas space. We have verified mapping accuracies for known neurons and demonstrated the usefulness of this platform to reveal unknown neuronal distributions. Together, these tools provide high-throughput analyses of whole mouse SC and enable direct comparison of 3D spatial information between animals and studies.

INTRODUCTION

The spinal cord (SC) integrates sensorimotor signals that ultimately produce the precise patterns of motor activity that control movement. Spinal neurons (SNs) receive and process somatosensory signals from skin, muscles, joints, and viscera and direct local and brain-derived motor commands. A huge body of work has provided a good understanding of the roles of major SN types in sensorimotor processing and there are now many examples of well-characterized neurons whose morphology, position, interconnections, and functions are known within defined segments of SC. Emerging from this work is the importance of stereotypic positioning of SNs as a basis of circuit specificity, in the transverse plane, dorsoventrally (d-v), and mediolaterally (m-l), and along the axis of the SC, rostrocaudally (r-c), to accommodate distinct body regions. Current knowledge comes from classical *in vivo* electrophysiology and anatomy and from work exploring the genetic bases of SC development and the specification of cell types (Abraira and Ginty, 2013; Brown, 1982; Gatto et al., 2019; Goulding, 2009; Jessell, 2000; Lai et al., 2016; Osseward et al., 2021; Rexed, 1954; Sherrington, 1906; Stachowski and Dougherty, 2021; Tripodi et al., 2011). These studies have also produced genetic markers for identifying and tracing cell development and for manipulating neuronal function in subsets of SNs. Recently, advances in single-cell transcriptional profiling have revealed a further level of cellular heterogeneity within the cardinal classes of SNs (Delile et al., 2019; Häring et al., 2018; Osseward et al., 2021; Rosenberg et al., 2018; Sathyamurthy et al., 2018) and in turn demand finer delineation of neurons and their connections for our understanding of the cellular architecture of functional circuitry. While molecular insights and the precision of modern genetic tools provide the means to access and label increasingly specific subsets of SNs, positioning such data in relation to other neurons and circuits within the framework of the whole SC has been elusive, as we lack tools for 3D analysis of whole mouse SC.

Visualizing cells and connections in a structure that, in mouse, spans 3–4 cm is technically challenging. Traditional histological approaches are prohibitively labor intensive; manually collecting, staining, and imaging several hundred sections while maintaining

r-c order is painstaking and the lack of tools for 3D reconstruction and analysis within a standardized reference limits data comparison. In an alternative approach, two-photon microscopy has been used to visualize axons in superficial layers of intact whole SC, but myelinated fiber bundles hinder deep imaging (Hilton et al., 2019; Johannssen and Helmchen, 2013). Tissue clearing (reviewed in Tian and Li, 2020; Ueda et al., 2020), in combination with light sheet microscopy, has enabled fast, 3D visualization of large intact samples (Cai et al., 2019; Hillman et al., 2019; Pan et al., 2016; Zhao et al., 2020). However, while clearing has been used effectively to visualize genetically labeled spinal tracts (Ertürk et al., 2012a; Hilton et al., 2019), complete clarity in mature SC remains elusive due to the abundant myelin that introduces light scattering (Soderblom et al., 2015). Moreover, solvent-based clearing methods are often incompatible with endogenous protein fluorescence (Ertürk et al., 2012b; Pan et al., 2016; Qi et al., 2019; Renier et al., 2014) and lipophilic tracers or DNA dyes (Tian and Li, 2020). Aqueous- and hydrogel-based methods that preserve protein-based fluorescence are limited by antibody compatibility and low penetration rates (Tian and Li, 2020), and in fact, whole adult SC is too large to be cleared or processed for immunohistochemistry (IHC) using these protocols (Vigouroux et al., 2017). Thus, there remains a pressing need for alternative methods to produce whole-SC 3D image datasets.

A second problem is that, regardless of acquisition method, resources for analyzing whole-SC data are scarce and lag far behind the manifold tools available for whole-brain reconstruction, atlas registration, and data interpretation (Bakker et al., 2015; Botta et al., 2020; Chon et al., 2019; Eastwood et al., 2019; Friedmann et al., 2020; Oh et al., 2014; Puchades et al., 2019; Shiffman et al., 2018; Tappan et al., 2019; Tyson et al., 2021; Wang et al., 2021). 3D reconstruction and analysis of human SC MRI data has been reported, but the tools offer only low-resolution data registration of larger gray matter (GM) and white matter (WM) regions (De Leener et al., 2017; Prados et al., 2016). To advance this field of research, we require a fully annotated, digital 3D SC reference atlas for interpretation and comparison of data in mouse, the most widely used model of spinal circuit formation, somatosensory and motor behavior, axon regeneration, and SC injury.

Here, we present accessible tools for efficient analysis of labeled cells and projections in whole mouse SC in the context of a novel 3D anatomical atlas that provides a common spatial framework for all studies. We have developed methods for oriented and parallel embedding of serial tissue pieces of the entire SC within a single block permitting controlled, synchronous cryo-sectioning and automated imaging of sections. We have also developed software, SpinalJ, to sort and register section images and to map the reconstructed data to a prototype 3D reference atlas. SpinalJ further combines tools for manual and automated analysis of identified cells and projections, and for data visualization. As an open resource, SpinalJ provides the community with high-throughput comparative analyses of SNs and their projections in whole SC.

RESULTS

Efficient embedding and sectioning of whole SC

For efficient *in toto* IHC- or other label-based analysis of the SC, we first sought to reduce sectioning and processing time, in a way that maintains r-c section order and facilitates automatic image acquisition.

Dividing SC tissue for synchronous and ordered sectioning

Sectioning the cervical to lumbar region of adult mouse SC at 25 μm produces ~1,200 tissue sections. To reduce sectioning effort, we divided the tissue into nine consecutive pieces and embedded them in parallel in the same block for synchronous sectioning (Figure 1A). This approach offers dense, regular spacing of tissue sections on the slide allowing for automated imaging and also saving time and materials for subsequent IHC processing. The fixed, cryo-protected SC was first cut into three equal pieces that together cover the cervical to lumbar extent of SC (Figure 1B). Each of these pieces was then further divided equally into three (Figures 1C and 1D).

SpineRacks

To facilitate fast, accurate, and reproducible arrangement of the nine SC tissue pieces in an upright orientation, we developed 3D-printed, water-soluble polyvinyl alcohol (PVA) support scaffolds, here termed SpineRacks. SpineRacks fit into 12-mm embedding molds and offer nine wells arranged in a 3 × 3 grid (Figure 1E). After immersion of the SpineRack in a mold filled with optimal cutting temperature embedding compound (OCT), SC tissue pieces were easily guided into the wells with forceps (Figures 1F–1I). The walls of the well act as flow barriers, preventing already positioned segments from drifting in the viscous OCT as other segments were being placed, so as to maintain upright orientation during block freezing.

We chose PVA for production of SpineRacks because it is soluble in water and would be expected to dissolve slowly in aqueous embedding medium like OCT, offering two major advantages. First, while providing mechanical support to hold embedded tissue pieces in their orientation, the structure could be partially dissolved, and softened for smooth sectioning, during incubation in OCT before freezing. OCT contains 10% PVA and we argued that the shared material properties between SpineRack and surrounding embedding medium would establish a continuous matrix, further promoting smooth sectioning. Second, after sectioning, SpineRack material, like OCT, could be washed away in PBS, eliminating any support components that might negatively affect staining protocols or contribute to background signals. Indeed, as predicted, SpineRacks dissolved in OCT (Figure S1) and the blocks sectioned smoothly, resulting in good tissue integrity.

Using SpineRacks, sectioning effort was reduced 9-fold: all ~1,200 sections from cervical, thoracic, and lumbar levels of one adult mouse SC were collected in only ~130 block sections (each with nine transverse SC sections) on ~16 slides (Figures 1J and 1K). Importantly, the precise arrangement of tissue sections on the slide permitted automating acquisition, ordering, and registration of images (see next section). Thus, processing of all sections can be achieved semi-automatically within a relatively short time (Table S1).

While our focus was on the reconstruction of the cervical to lumbar SC of a single animal, SpineRacks can also be used for other purposes; e.g., to process a single tissue region of

CellPress
OPEN ACCESS

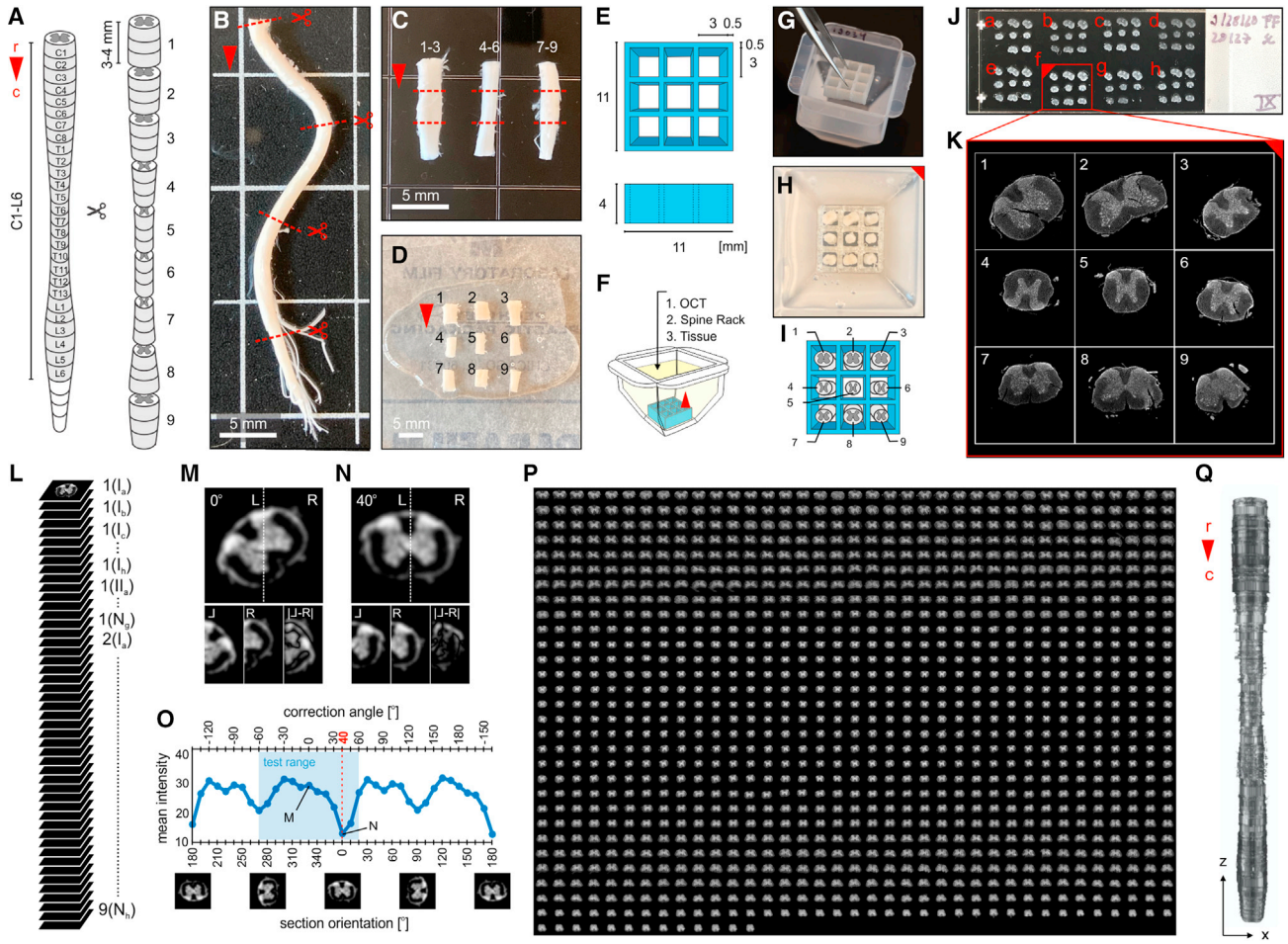

Figure 1. Embedding and sectioning of mouse spinal cord using SpineRacks and image processing and registration in SpinalJ

(A) Cutting scheme for synchronous sectioning of nine parallel embedded tissue pieces of the adult mouse SC. Red arrowhead in (A)–(D), (F) and (Q) indicates r-c orientation.

(B) The SC was divided into three equal pieces. Red dashed lines in (B) and (C) indicate cuts.

(C and D) Each piece was then split again into three (C), resulting in a total of nine pieces of SC (D).

(E) Design and dimensions of SpineRacks.

(F–H) For embedding (F), a SpineRack was sunk into a plastic mold filled with OCT (G; see also Figure S1) and SC pieces were placed into the wells of the rack, each with its rostral end facing down (H). Red-filled image corner indicates the orientation of the tissue block for tracking as in (J) and (K).

(I) Order of tissue pieces within the SpineRack. Pieces 1–3 were embedded left to right in the top row, 4–6 in the middle row, and 7–9 in the bottom row.

(J) Eight cryostat block sections (a–h) were collected in two rows (1–4, top left to right; 5–8, bottom left to right) on each slide (shown here as brightfield photo). In this arrangement, >1,000 sections of adult mouse SC fit on 16 slides.

(K) Each block section, comprising nine tissue sections, was scanned on a slide scanning microscope and saved as a single image file (here shown NT 640/660 signal). Images of block sections were ordered according to their position on the slide (A–H) to match sectioning sequence and segmented into nine individual tissue section images (1–9) in SpinalJ.

(L) Images were then sorted rostro-caudally. Section 1, slide I, block a = 1(Ia).

(M and N) For horizontal alignment of sections (M), images were centered and thresholded using the NT or DAPI (not shown) channel. The resulting image was split vertically (dotted line) and the left half (L) was mirrored and overlaid with the right half (R) to calculate the average intensity of the absolute difference of both images (|L-R|). This value was minimized when both image halves aligned perfectly, indicating horizontal orientation (N).

(O) To determine horizontal orientation for each section automatically, images were rotated by increments of 10° from −60° to +60° (reflecting the range of typical embedding orientations; blue shaded area) and the angle resulting in the lowest mean difference intensity was applied to align the section.

(P) Montage of 1,086 sorted and aligned images of a sample spanning C1–S1.

(Q) Dorsal view of the 3D reconstructed dataset (NT channel) shown in (P) after section registration.

interest (e.g., L3–L6) from multiple animals in parallel. SpineRacks with similar or adjusted geometries can also be used for efficient and oriented sectioning of a variety of other tissues that are difficult to embed because of their low width-to-length ratio, such as muscle or whole organisms like fish and insect larvae. We have used SpineRacks for parallel sectioning of multiple fish brains (Figure S2) and precisely oriented adult mouse eyes (Figure S3).

Reconstruction of 3D image data from sections

We have developed SpinalJ, a plugin for ImageJ, which combines a series of software tools into a seamless open-source pipeline that implements image registration, atlas mapping, and 3D analysis of SC sections. SpinalJ was conceived with reference to our toolbox for the registration and analysis of brain sections, BrainJ (Botta et al., 2020), but with a new pre-processing workflow to process section arrays, a novel 3D SC atlas, and additional mapping and analysis options.

Image pre-processing in SpinalJ

For best flexibility and to accommodate various formats of input data, the image pre-processing workflow in SpinalJ has been organized in modules that can be executed independently as outlined below:

(1) Utilizing the ordered array of SC tissue embedded in SpineRacks, SpinalJ automatically segments block section images that contain nine tissue sections into individual section images (Figure 1K). Block section images that contain fewer than nine tissue sections cannot be segmented automatically but simple manual placement of a segmentation mask on a preview displayed in SpinalJ solves this issue.

(2) To maintain continuity within the 3D space of whole SC, SpinalJ uses the positional information of a list of sections that were lost during sectioning or washing to replace them by duplicating neighboring sections, thereby compensating for gaps in the image data (in our hands, <15% of total images).

(3) Controlling d-v orientation of SC tissue pieces during embedding can be challenging, especially for thoracic segments. SpinalJ automatically aligns sections horizontally (see next section), but approximate d-v orientation is required. Sometimes it is necessary to re-orient all sections from a tissue piece. SpinalJ creates a preview of all section images sorted by piece and the user can manually select pieces for re-orientation.

(4) For r-c sorting of images, SpinalJ uses either the alphanumeric order of image filenames or stage coordinate information extracted from image metadata (Figure 1L). For successful registration, the image dataset has to be free of sections that are damaged or out of focus and empty images. To clean the dataset, SpinalJ displays a preview of each section and the user selects whether to keep (intact), replace with the neighboring section (damaged/out of focus), or delete (empty) images.

(5) Horizontal alignment of SC sections optimizes the registration process leading to final 3D reconstruction. We found that classical approaches to achieve horizontal alignment, like ellipse fitting (Pratt, 1987), did not perform well because SC sections differ dramatically in shape along the r-c axis (from highly elliptic to near round). Instead, we developed a method based on the bilateral symmetry of the GM, marked by fluorescent Nissl (Neurotrace [NT]; Quinn et al., 1995) or DAPI, to determine orientation. Sections were centered and the NT/DAPI channel of images was thresholded and smoothened by Gaussian filtering. The image was then split vertically and the left half (L) was mirrored to match the orientation of the right half (R). The average intensity of the absolute difference of both images was then calculated (|L-R|, Figure 1M, shown for NT). This value is minimized when the halves are mirror symmetrical, indicating horizontal orientation (Figure 1N). For automated horizontal alignment, SpinalJ rotates section images by increments of 10° from −60° to +60° (covering the range of typical embedding orientations) and the angle at the intensity minimum is used to rotate the section (Figure 1O). Note that the distribution of mean difference intensities across all rotation angles has additional minima at ±90° and ±180° orientation. To ensure proper d-v alignment, sections oriented >90° and <−90° (upside down) must be coarsely aligned, manually, first (see step 3).

Section registration in SpinalJ

Image pre-processing in SpinalJ produces a continuous stack of consecutive, intact tissue sections in r-c order (Figure 1P). To reconstruct a 3D dataset from these sections, a rigid body registration that preserves the shape of the tissue sections (Thévenaz et al., 1998) was performed on a contrast-enhanced and down-sampled (10 μm/pixel) copy of the registration channel (DAPI and NT were both found to be suitable for this purpose). The re-scaled transformations were subsequently applied to all channels at the desired resolution for analysis (typically 2 μm/pixel), which yielded a registered 3D volume (Figure 1Q).

Creation of a 3D reference atlas for mouse SC

Comparative analysis and interpretation of whole-SC data from registered sections requires a standard framework. We have therefore built a 3D atlas for mouse SC using, as a base, the 34 annotated 20 μm sections (one for each spinal segment) of the Allen Spinal Cord Atlas (ASCA; Allen Institute for Brain Science, 2008) (Figures 2A and 2B) in the following steps:

(1) We digitized a total of 73 regions within the ASCA using an intensity map (Figure 2C). These annotated section images, and their corresponding Nissl images, were then manually edited to be symmetrical and free from idiosyncratic features or damage that may impair their use as a template for registration.

(2) The Nissl images were used to generate a 3D volume. Images were next processed using attenuation correction to compensate for section-to-section intensity variations and were then aligned using rigid body registration (Thévenaz et al., 1998). Images typifying each SC segment were then stacked with a spacing of 20 μm to fill the average length of each spinal segment (Figure 2D). Segment lengths and the position of segment boundaries were determined, informed by the positions of sections chosen within the ASCA and by the relative lengths of segments as reported in the literature (Harrison et al., 2013) (Figure 2F). This 3D template was used to align all experimental datasets.

(3) To complete the atlas, the transformation parameters obtained from registering Nissl sections were applied to the

CellPress
OPEN ACCESS

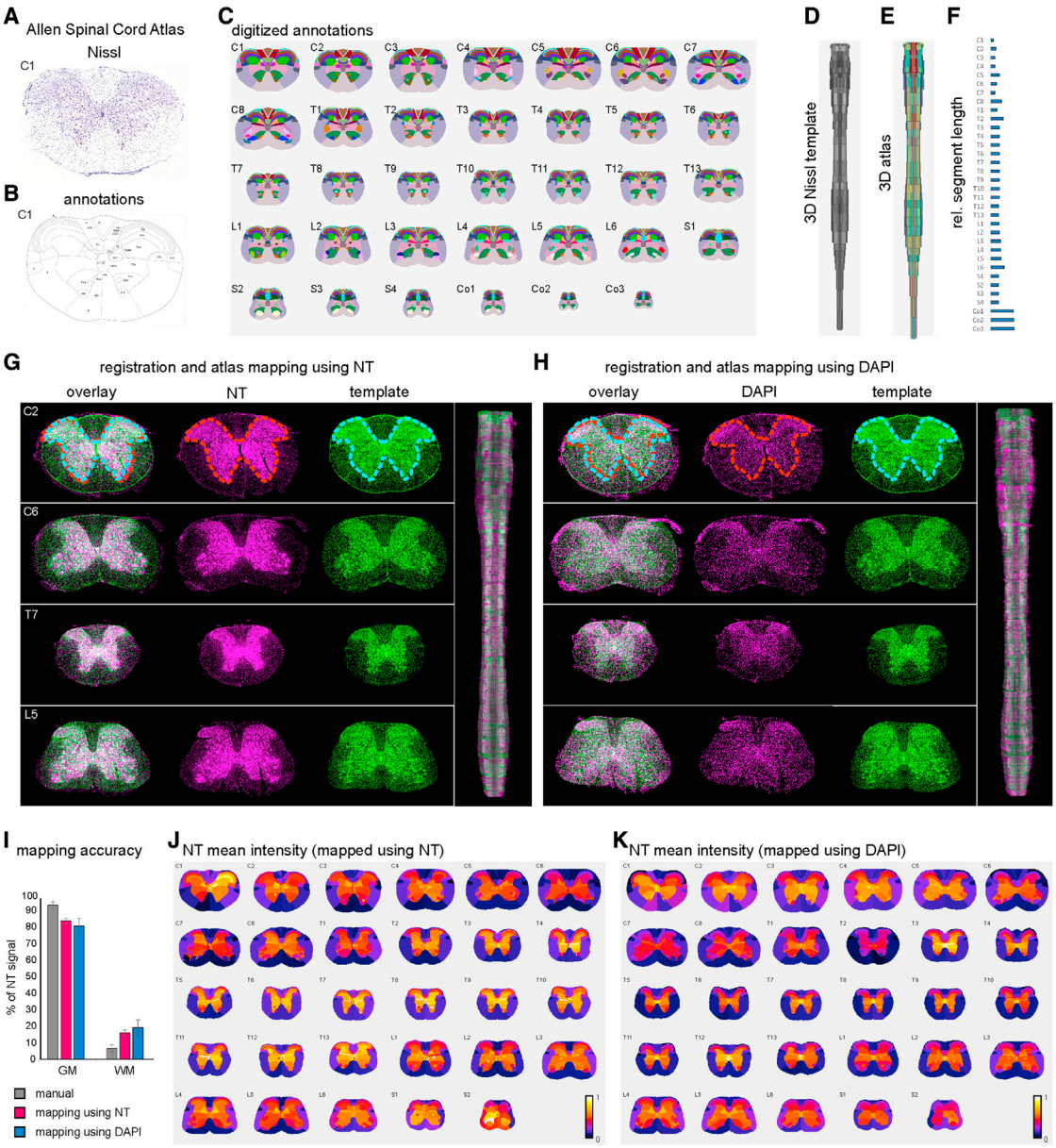

Figure 2. Mapping registered SC sections to a novel 3D atlas in SpinalJ

(A and B) Creation of the 3D reference atlas used 34 Nissl-stained sections (A) (shown for C1) and corresponding annotated sections (B) of the ASCA (Allen Institute for Brain Science, 2008).

(C) Digitized annotations of all sections (one for each SC segment, C1–Co3).

(D) A 3D Nissl template (dorsal view) was created by registering and extruding the sections representing each segment.

(E) The transformation to create (D) was then applied to the annotated sections (C) to generate a 3D annotated atlas.

(F) Segment boundaries were placed according to the relative positions of sections in the ASCA and the relative lengths of segments (blue bars) as reported in the literature (Harrison et al., 2013).

(G and H) Example of mapping the same experimental dataset (magenta) to the Nissl template (green) using either (G) NT or (H) DAPI. Dashed lines indicate GM/WM boundary in C2.

(I) Distribution of NT signal between GM and WM along the entire SC of four animals, measured manually (gray bar) and after SpinalJ atlas mapping using NT (magenta bar) or DAPI (blue bar). NT signal in GM: 93.68% (manual), 84.09% (±1.73%) (NT), 80.92% (±4.76%) (DAPI). NT signal in WM: 6.32% (manual), 15.91% (±1.73%) (NT), 19.08% (±4.76%) (DAPI). Error bars = SD. With reference to manually determined signal distributions, SpinalJ mapping accuracies were 89.76% (NT) and 86.37% (DAPI), respectively.

(J) Heatmaps of mean NT intensity distribution after template mapping with NT, summarized for each segment.

(K) Heatmaps of mean NT intensity distribution after template mapping with DAPI.

digital annotation images (Figure 2E). For convenient analysis in SpinalJ, we created additional atlas region groups, combining individual annotated regions into relevant quantification clusters (e.g., region group "Lamina V" combines atlas regions 5Sp, 5SpL, 5SpM, D, SDCom, CeCv, and IMM5). These calculated region groups allow users to evaluate data at different levels of anatomical detail (Table S2).

Atlas mapping

Atlas mapping in SpinalJ brings experimental data into anatomical context by mapping the registered sections to the 3D Nissl template and overlaying them with the 3D annotations for analysis. SpinalJ first resamples the registration channel of the experimental data to match the resolution and relevant segment range of the atlas template. Registration of the resampled data to the template is achieved using Elastix (Klein et al., 2010). Briefly, a 3D affine transformation followed by a 3D B-spline transformation is performed using Mattes Mutual Information.

To validate atlas mapping using NT or DAPI for registration and atlas mapping, we inspected the alignment of GM and WM regions between experimental data and template. Visual inspection using either marker showed good alignment (Figures 2G and 2H). To assess the mapping accuracy quantitatively, we first manually outlined the GM and WM in 39 randomly selected sections from four animals and determined mean intensities of thresholded NT signal in each region. NT binds the ribosomal RNA associated with the rough endoplasmic reticulum in neuronal soma and dendrites (Quinn et al., 1995) and signal should thus be restricted to the GM. Indeed, we found strong signal in the GM of sections stained with NT660 (93.68% of total NT signal, N = 4, n = 39), and only sparse, punctate signal in the WM (6.32% of total NT signal) (Figure 2I). We then compared these manual values with those determined automatically by atlas mapping using SpinalJ. We found that, across all spinal segments, 84% of NT signal was mapped to the GM and 16% to the WM, when using NT for section registration and mapping (Figures 2I and 2J), indicating a mapping accuracy of 90%. Mapping was slightly less accurate using DAPI (86%) for registration and atlas mapping, with 81% of NT signal in the GM and 19% in the WM (Figures 2I and 2K). Thus, SpinalJ offers highly accurate template mapping of 3D reconstructed sections.

Analysis of cells and projections

For the analysis of position and connectivity of SNs within the atlas, SpinalJ offers options to detect cells and projections automatically, via image segmentation. The quickest and simplest segmentation method, binary thresholding, applies a user-specified intensity threshold to separate signal from background. To tune the detection of cells, "find maxima" isolates the positions of local intensity maxima around a user-specified intensity value. Most detailed segmentation, machine learning segmentation, for detection of both cells and neurites, is based on distinct pixel probabilities derived from training pixel classifiers using Ilastik (Berg et al., 2019). SpinalJ can also import a list of manually determined coordinates. All approaches allow for additional filtering based on intensity and object size. Extracted coordinates are then transformed into SC atlas space, and reverse mapping is used to measure cell and projection density within annotated regions. SpinalJ outputs these data in both table and image formats for easy exploration. To test the mapping accuracy of SpinalJ, we analyzed labeled neurons with well-characterized distributions within sub-regions of the SC.

Mapping of neuronal position

To validate cellular mapping, we labeled SC sections with an antibody against choline acetyltransferase (ChAT), a marker for cholinergic SNs (Figure 3A). The distribution of ChAT in adult SC has been described; it is restricted to motor neurons (MNs) of lamina IX, neurons in the intermediolateral column, the intercalated nucleus, the sacral parasympathetic nucleus and medial part of lamina VII, the central autonomic area, and the central canal cluster neurons of lamina X, as well as in laminae III–V of the dorsal horn (DH) (Barber et al., 1984; Heise and Kayalioglu, 2009). To assess the distribution of ChAT signal after atlas mapping, SpinalJ determined the mean intensity of ChAT signal per atlas region for each segment. The mapped intensity data were then visualized as intensity heatmaps (Figure 3B). This analysis demonstrated that signals map predominately to the ventral GM regions of SC. To visualize the data within larger region groups across segments, we generated heatmap matrix plots, which showed highest intensities in laminae VII, IX, X, and also VIII (Figure 3C). Additionally, lower-intensity signals were mapped to more dorsal laminae, where visual inspection revealed background fluorescence but only a few $ChAT^+$ cells.

While mapping mean intensities is the fastest way to analyze data in SpinalJ, we extracted features of interest and eliminated background using automatic machine learning image segmentation to refine the analysis (Figures 3D and 3E). After initial training, segmentation parameters can be applied to multiple datasets for high throughput. We validated the accuracy of this method by comparing the overlay of detected cells and raw ChAT signal (Figures 4A and 4E). In 20 randomly selected sections, 89% of labeled cells were detected, attesting to the accuracy of this segmentation approach. The coordinates of identified cells were then used to calculate cell densities within each atlas region (Figures 3F and 3G). This approach provided a much clearer distribution of $ChAT^+$ cells than is found with intensity mapping (Figure 3H) and reproduced the known distribution, with the exception of cells mapped to lamina VIII (potentially as a result of imprecise lamina IX annotations; see discussion). Cell densities were greatly reduced in laminae I–VI and X, indicating that mean intensity mapping included non-cellular/background signal. These results illustrate the usefulness of mean intensity mapping for quick analysis of overall signal distribution and further refinement using more detailed segmentation approaches.

Mapping of peripheral fiber terminals

Next, we tested the detection and mapping accuracy of projections. We labeled sections with Isolectin B4 (IB4), which binds non-peptidergic dorsal root ganglion neurons and their afferents. These innervate primarily the inner part of lamina II (IIi) and, to a lesser extent, lamina II outer (IIo) (Molliver et al., 1995; Silverman and Kruger, 1990; Takazawa et al., 2017).

Mapping of IB4-FITC signal showed highest mean intensities in the superficial DH at all r-c levels (Figures 4A and 4B). Although the highest intensities were observed in laminae I and II, lower

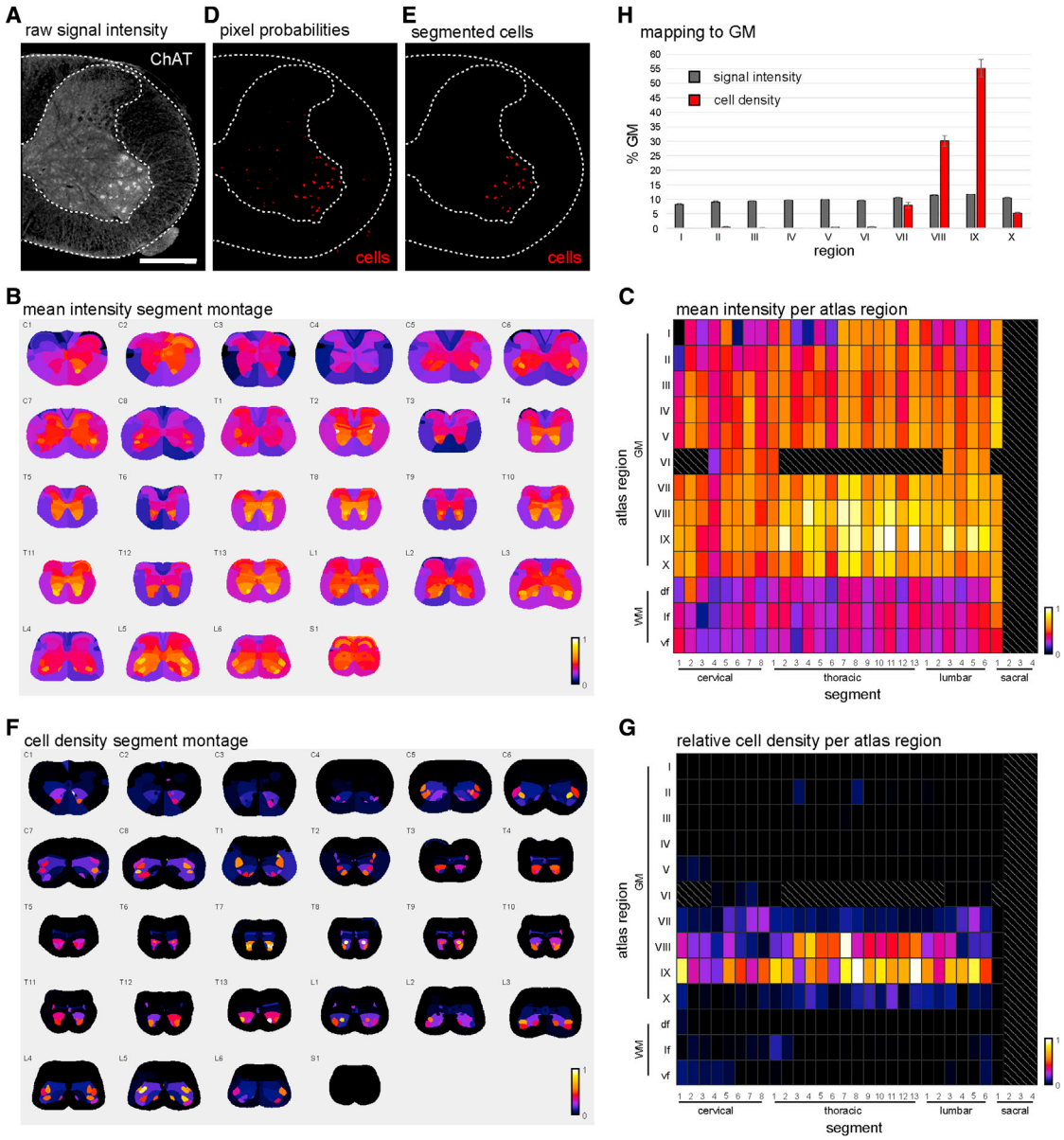

Figure 3. Intensity and cell density mapping of ChAT⁺ SNs

(A) Hemisegment of SC section labeled with ChAT antibody. Scale bar, 500 μm.

(B) Heatmap montage showing the spatial distribution of mean ChAT intensity per atlas region and segment.

(C) Heatmap matrix plot showing the distribution of mean ChAT intensity in atlas region groups of the GM (laminae I–X) and WM (df, dorsal funiculus; lf, lateral funiculus; vf, ventral funiculus).

(D) Pixel probabilities for classifier cells (red) after training in Ilastik.

(E) Cells detected after image segmentation using pixel probabilities.

(F) Spatial distribution of relative ChAT⁺ cell density per atlas region and segment.

(G) Heatmap matrix plot showing the distribution of relative ChAT⁺ cell density in atlas region groups. Gray hatched areas in (C) and (H) mark regions without data.

(H) Relative distribution of ChAT signal intensities (gray bars) and cell densities (red bars) within atlas regions of the GM (laminae I–X). Error bars = SD between values from both hemisegments.

but significant signal was also detected in laminae III and IV–X (Figure 4C), suggesting mapping of background signal. Analysis of projection densities after machine learning image segmentation (Figures 4D and 4E) revealed that the highest densities were mapped to lamina II (Figures 4F and 4G). In contrast to mean intensities, projection densities in laminae I and III were significantly lower than in lamina II (reduced by 19.0% and 18.5%, respectively) and close to zero in laminae IV–X

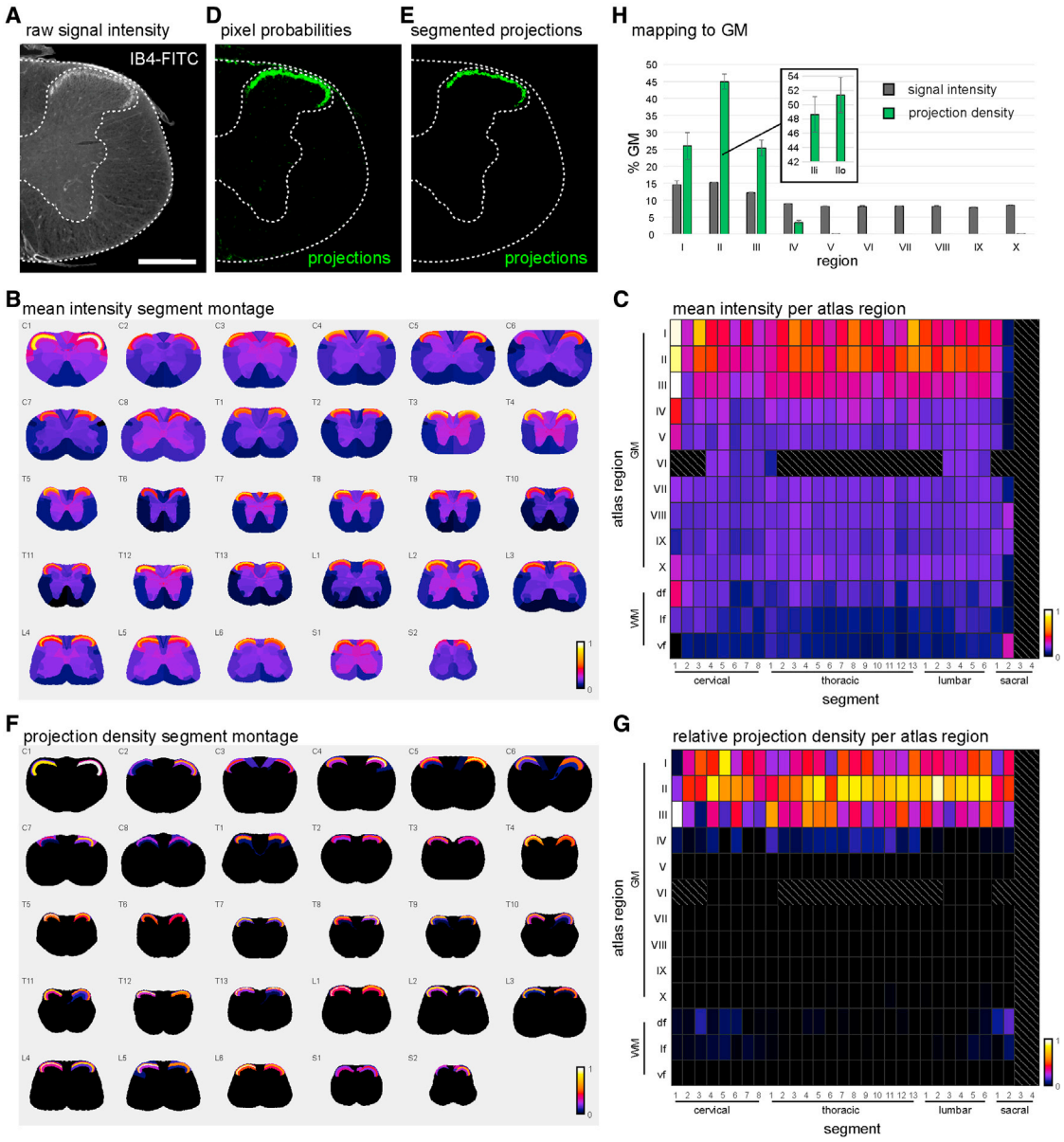

Figure 4. Intensity and projection density mapping of IB4^{+} fibers

(A) Hemisegment of SC section labeled with IB4-FITC. Scale bar, 500 μm.

(B) Spatial distribution of mean IB4 intensity per atlas region and segment.

(C) Distribution of mean IB4 intensity in atlas region groups of the GM (laminae I–X) and WM (df, dorsal funiculus; lf, lateral funiculus; vf, ventral funiculus).

(D) Pixel probabilities for classifier projections (green) after training in Ilastik.

(E) Projections detected after image segmentation using pixel probabilities.

(F) Spatial distribution of relative projection density per atlas region and segment.

(G) Distribution of relative projection density in atlas region groups. Gray hatched areas in (C) and (H) mark regions without data.

(H) Relative distribution of IB4 signal intensities (gray) and projection densities (green) within atlas regions of the GM (laminae I–X). Inset shows projection densities within laminae II (IIi and IIo). Error bars = SD between values from both hemisegments.

(Figure 4H). Within lamina II, we found slightly higher densities in lamina IIi compared with lamina IIo, although this trend was not statistically significant (Figure 4H, inset). Thus, SpinalJ performs well in mapping axon terminals and is able to isolate signals of particular interest using segmentation.

Mapping of long-range projections

To test the ability of SpinalJ to map axonal projections over long r-c distances and seamlessly across multiple segments, we labeled axons of the corticospinal tract (CST) by unilateral injection of AAV-tdTomato into the cortex of an adult mouse

CellPress
OPEN ACCESS

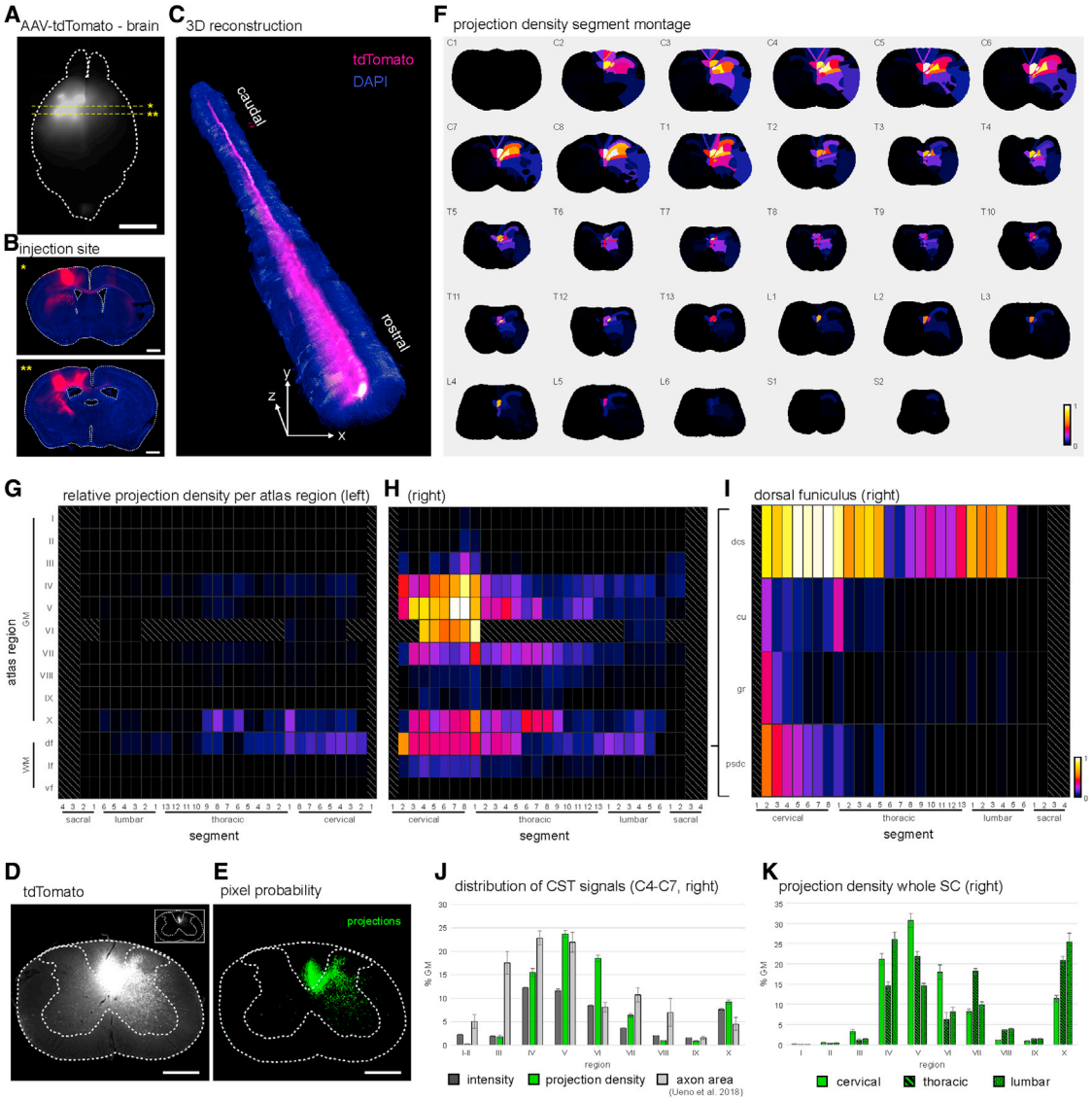

Figure 5. Intensity and projection density mapping of AAV-labeled CST axons

(A) tdTomato signal in a dorsal view of the brain shows AAV-tdTomato injection sites in left sensory and motor cortex. Yellow dotted lines indicate positions of sections shown in (B). Scale bar, 3 mm.

(B) Coronal sections of the brain at levels indicated in (A), showing tdTomato (red) and DAPI (blue). Scale bar, 1 mm.

(C) 3D reconstruction of registered SC sections. Image shows the 3D dataset (composite of tdTomato [magenta] and DAPI [blue]) in a frontal and dorsal view.

(D) Cervical SC section showing the distribution of tdTomato signal. Inset shows same image reduced in brightness. Scale bar, 500 μm.

(E) Pixel probabilities for classifiers projections (green) after training in Ilastik.

(F) Spatial distribution of relative projection density per atlas region and segment.

(G and H) Distribution of relative projection density in atlas region groups of the GM (laminae I–X) and WM (df, dorsal funiculus; lf, lateral funiculus; vf, ventral funiculus) within the left (G; ipsilateral) and right (H; contralateral) hemisegments. Gray hatched areas mark regions without data.

(I) Distribution of relative projection density in atlas regions within the df of the right hemisegment (dcs, dorsal corticospinal tract; gr, gracile fasciculus; psdc, postsynaptic dorsal column pathway; cu, cuneate fasciculus). See also Figure S4.

(J) Relative distribution of mean intensities (dark gray bars) and projection densities (green bars) within atlas regions of the GM of segments C4–C7. Light gray bars show the relative distribution of CST axon area as measured in a manual mapping study (Ueno et al., 2018). Error bars = SD of values from all segments within the analyzed range.

(K) Distribution of relative projection densities within atlas regions of the GM of cervical (plain green bars), thoracic (diagonally banded bars), and lumbar (checkerboard patterned bars) segments. Error bars = SD of values from all segments.

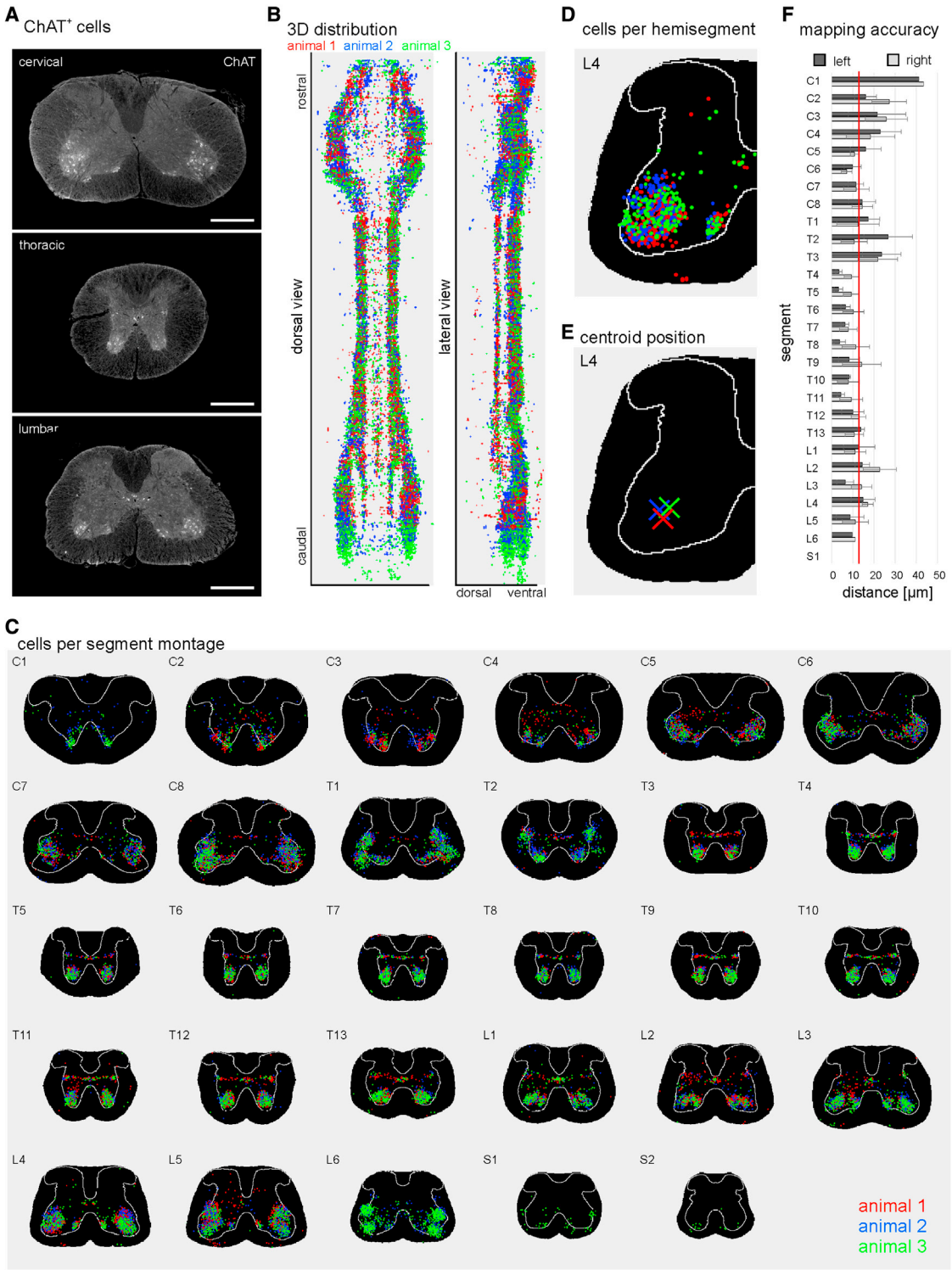

Figure 6. Mapping ChAT cells in multiple animals

(A) Sections labeled with anti-ChAT antibody. Scale bar, 500 μm.

(B) 3D distribution of the positions of ChAT$^+$ SNs detected in three different samples (animals 1–3, red, blue, green) in a dorsal (left) and lateral (right) view. See also Figure S5.

(C) Spatial distribution of ChAT$^+$ SNs from different samples within each segment.

(legend continued on next page)

(Figures 5A and 5B). We determined the position of injection sites and found tdTomato$^+$ neurons in the primary and secondary motor area (n = 2,367, 60% total labeled cells), primary somatosensory area (n = 1,022, 26%) and anterior cingulate area (n = 513, 13%), with few cells (n = 22, 1%) in non-CST regions (mainly CA2 and CA3) of the left hemisphere. Thus, 99% of labeled neurons were located within nuclei that contribute to CST.

In cervical SC, CST neurons have been reported to innervate laminae III–VIII and lamina X of the contralateral GM (Ueno et al., 2018). After section registration in SpinalJ, the 3D reconstruction of our data showed a continuous CST with lateral branches innervating the DH (Figure 5C). Analyzing the distribution of projection densities (Figures 5D and 5E), we found high densities in laminae IV, V, and VI of the contralateral GM, with lower densities in laminae III, VII, and X (Figures 5F–5H). In the WM, the highest projection densities were found in the contralateral dorsal funiculus (df, Figure 5H) and, within the df, projections concentrated in the dorsal CST region (dcs, Figure 5I). Low densities were also seen in lamina X and df of the ipsilateral hemisegment. In all regions, projection densities declined caudally, reflecting the thinning of the CST. Mapping mean signal intensities showed overall similar signal distributions (Figure 5J).

Both of our analyses revealed signal distributions that closely matched the results of a manual mapping study on segments C4–C7 (Ueno et al., 2018) (Figure 5J, light gray bars), validating SpinalJ mapping. A major advantage of analysis of whole SC in SpinalJ is that the entire projection can be visualized and projection densities measured at all spinal levels simultaneously (Figure 5K). Moreover, the ability to segregate features such as bright axon bundles (Figure S4A) and dimmer lateral branches (Figure S4B) in the same image channel using Ilastik is a powerful option for selective mapping of features of interest (Figures S4C and S4D). This principle of using segmentation in SpinalJ can be applied also to discriminate morphologically distinct compartments of SNs. For example, soma and neurites can be analyzed separately in the same image channel, as demonstrated (Figures S6A–S6E). The quick assessment of axonal tracts and terminations in 3D using SpinalJ provides a new approach to studying SC connectivity and regeneration of axons after injury.

Mapping and comparing multiple samples

Accuracy of mapping the same cell population across samples

The approach of mapping section data to a standardized template in principle permits the comparison of spatially discrete populations of SNs across different animals. To assess the alignment accuracies of multiple datasets, we mapped and compared the positions of ChAT$^+$ neurons (Figure 6A) from three SCs. For this, we plotted the 3D cell positions, color coded for each animal, and found that the overall 3D distribution of cells was represented in each sample (Figure 6B). Color coding cells by atlas region revealed the reported columnar organization of ChAT$^+$ MNs and showed expected distributions of non-motor ChAT$^+$ SNs along the central canal (V0c) and in the DH (Figure S5). To quantify inter-animal mapping differences within each spinal segment, we projected the cell position data of each segment along the r-c dimension (Figure 6C). We then calculated the center of mass (centroid) of the transverse 2D cell distribution within each hemisegment and spinal level for each animal (Figures 6D and 6E). Next, we calculated and averaged the pairwise distances between all centroids as an indication of mapping precision. Between animals and across all spinal levels we found an average centroid distance (mapping disparity) of only ~13 μm (Figure 6F). Thus, mapping data from different animals can be accurately achieved in SpinalJ.

To test SpinalJ's ability to delineate cell populations with unknown distributions, we chose to map the subset of MNs that derive exclusively from progenitors expressing the Forkhead domain transcription factor 1 (Foxp1). These include the cholinergic neurons of the embryonic lateral motor column (LMC) and the preganglionic motor column (PGC) of lamina IX (Dasen et al., 2008; Morikawa et al., 2009), but they have not been mapped in the adult, since Foxp1 is also expressed in other SNs, precluding selective MN labeling. To characterize the 3D distribution of cholinergic Foxp1 MNs in the adult, we used a new intersectional mouse line that expresses tdTomato in VAChT$^+$, Foxp1$^+$ neurons (D.N., unpublished data). Mapping VAChT$^+$/Foxp1$^+$ cells using automatic cell detection in SpinalJ revealed large clusters of cells in ventrolateral SC at limb levels within the annotations of the LMC (Figures 7A and 7B, black arrowheads; Figure S6). In each hemisegment, an additional, thinner cluster of cells was observed extending caudally from cervical LMC and spanning the intermediolateral thoracic and upper lumbar segments as part of the PGC (Figures 7A and 7B, white arrowheads; Figure S6). These findings were in line with the expected distributions of these cells (Figure 7C). In the embryo, LMC neurons have been identified only at limb levels, whereas PGC neurons were also found in thoracic and upper lumbar segments T1–L2 (Jessell, 2000; Prasad and Hollyday, 1991; Stifani, 2014; Tsuchida et al., 1994). Surprisingly, we also observed a smaller cluster of cells in the extreme ventral horn of thoracic segments within the annotations of the hypaxial motor column (HMC) and median motor column (MMC) (Figures 7A and 7B, yellow arrowheads; Figure S6), regions not previously thought to include any cholinergic Foxp1 lineage neurons (Stifani, 2014). Minimal mapping offsets between samples (Figures 7B and 7D–7F) suggest that these cells were not mismapped. Moreover, we confirmed that these cells are indeed cholinergic by co-staining with ChAT antibody (Figures 7G–7J), ruling out the possibility of unspecific labeling or segmentation artifacts. Thus, using SpinalJ, we have mapped the 3D distribution of LMC and PGC MNs (amounting to 73% and 12% of all VAChT$^+$/Foxp1$^+$ cells; Figure 7K), and have also identified a previously undescribed population of cholinergic Foxp1$^+$ neurons (13%), which requires further characterization.

(D and E) Cell distributions within each hemisegment (shown for L4, left hemisegment; D) were analyzed to determine the centroid for each animal, spinal level, and hemisegment (shown for L4, left in E).

(F) Average pairwise centroid distances indicate mapping offset between animals within left (dark gray) and right (light gray) hemisegments at different spinal levels. Red line indicates average centroid distance across all segments (13.3 μm). Error bars = SD.

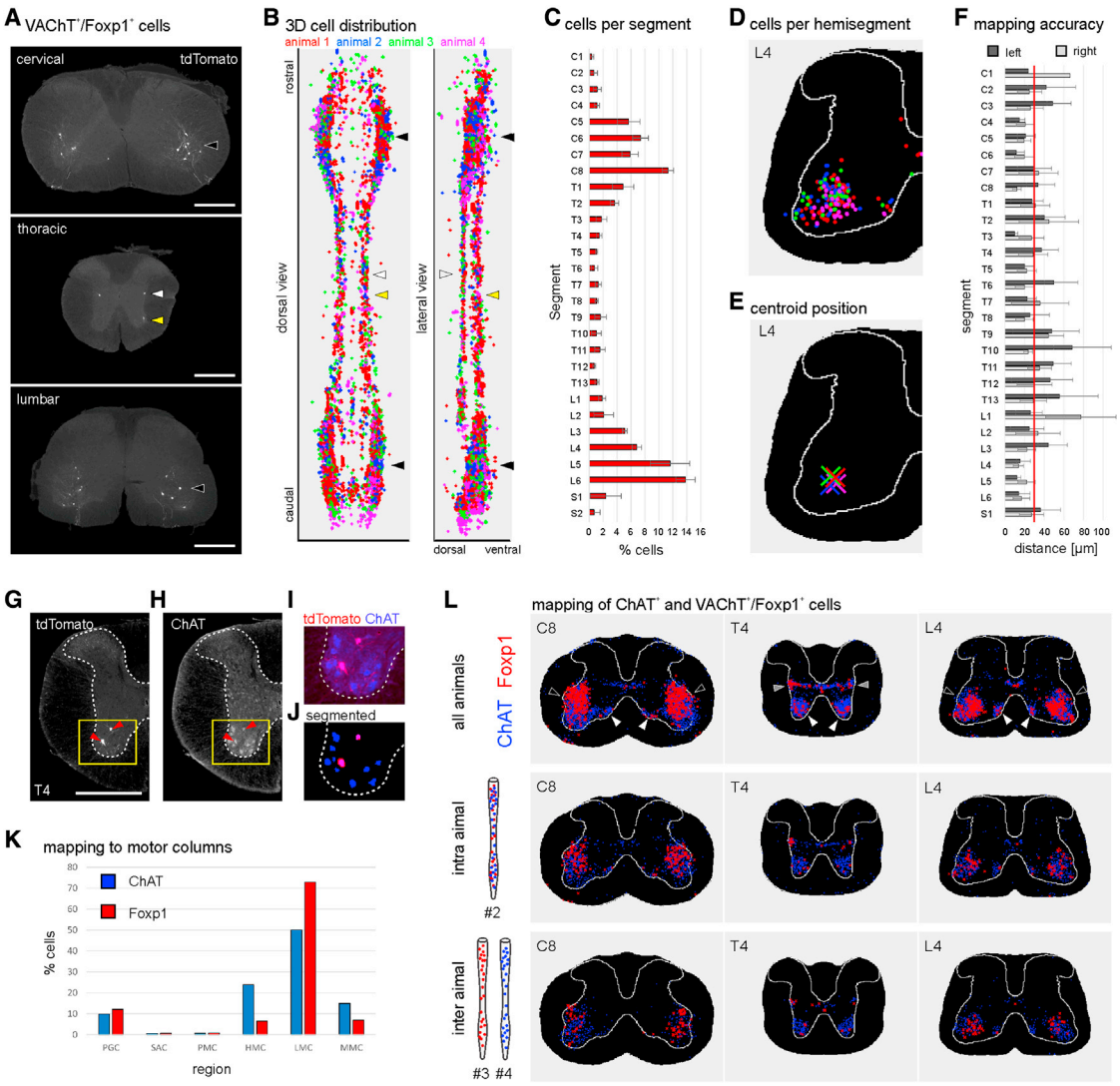

Figure 7. Spatial distribution of VAChT$^+$/Foxp1$^+$ cells and inter-animal mapping accuracy

(A) SC sections showing tdTomato$^+$ cells. Arrowheads mark cell clusters in the LMC (black), PGC (white), and HMC/MMC (yellow).

(B) 3D distribution of VAChT$^+$/Foxp1$^+$ (Foxp1) cells detected in four samples (animals 1–4, red, blue, green, magenta) in a dorsal (left) and lateral (right) view. Arrowheads mark motor columns as in (A). See Figure S6 for 2D distributions of cells in individual segments.

(C) Average number of Foxp1 cells per segment across all animals. Error bars = SD.

(D and E) Cell distributions within each hemisegment (shown for L4, left hemisegment; D) were analyzed to determine the centroid for each animal, spinal level, and hemisegment (E).

(F) Average pairwise centroid distances indicate the mapping offset between animals within the left (dark gray) and right (light gray) hemisegment at different spinal levels. Red line indicates the average centroid distance across all segments (30.3 μm). Error bars = SD.

(G) Section showing VAChT/Foxp1:tdTomato-labeled SNs (arrowheads) in T4. Scale bar, 500 μm.

(H) Anti-ChAT counterstaining of section in (A).

(I) Overlay of tdTomato (red) and ChAT (blue) signal from (G) and (H).

(J) Overlay of segmented tdTomato (red) and ChAT (blue) signals used for cell detection in the same field of view.

(K) Relative contributions of Foxp1 cells (red bars) and ChAT$^+$ cells (blue bars) to motor columns of four animals (SAC, spinal accessory motor column; PMC, phrenic motor column). *Foxp1*: LMC, 73%; PGC, 12%; HMC, 6%; MMC, 7%; SAC, 1%; PMC, 1%. *ChAT*$^+$: LMC, 50%; PGC, 7%; HMC, 25%; MMC, 15%; SAC, 1%; PMC, 2%.

(L) Top row: overlay of the positions of detected Foxp1 cells (red) and ChAT$^+$ cells (blue) at C8, T4, and L4 from all four animals. Arrowheads mark cell clusters in the LMC (black), PGC (gray), and HMC/MMC (white). Middle row: overlay of Foxp1 and ChAT$^+$ cell positions, measured in one animal (#2). Bottom row: overlay of cell positions from different animals: Foxp1 in animal #3, ChAT$^+$ in animal #4.

Mapping different cell populations across samples

The precise mapping of cells from multiple animals using SpinalJ also provides for close comparison of the relative positions of different cell populations. To test this, we plotted the positions of two different but overlapping sets of SNs: the cholinergic Foxp1 SNs (VAChT/Foxp1:tdTomato) and the entire cholinergic population of SNs (marked by anti-ChAT antibody). As expected, in four animals, all VAChT$^+$/Foxp1$^+$ cells lie within the distribution of the ChAT$^+$ cell population (Figure 7L, top row) and represent 20% of ChAT$^+$ neurons. Notably, the relative distributions of VAChT$^+$/Foxp1$^+$ and ChAT$^+$ cells matched closely, when comparing them in the same animal or across different animals (Figure 7K, middle and bottom rows), demonstrating the utility of SpinalJ for comparative analyses of relative spatial information in whole SC.

In summary, we provide a toolbox for the analysis of neurons and connections within the full r-c extent of mouse SC. We have developed SpineRacks for oriented embedding and efficient sectioning, SpinalJ for user-friendly image processing and analysis, and a 3D SC atlas that provides a standardized reference for analysis of cells and projections. We have validated the accuracy and reproducibility of SpinalJ mapping with reference to published manual studies, attesting to its usefulness for a variety of experiments. In addition, for the first time, the availability of a common coordinate framework and 3D anatomical annotations permits comparative mapping of SNs across samples and laboratories.

DISCUSSION

Given the technical limitations of traditional histological methods and more recent clearing approaches, SC analyses in mice have typically focused on intermittent sampling through the entire SC or on subsets of segments, resulting in incomplete characterization of the distributions and diversity of SNs and their projections along the r-c axis, as highlighted elsewhere (Francius et al., 2013). We developed SpineRacks as an efficient and inexpensive method to overcome the massive effort of ordered sectioning of entire mouse SCs, and now >1,000 25 μm sections can be collected on as few as 16 slides in under an hour. Moreover, ordered placement of tissue segments in SpineRacks made it possible to automate image acquisition, as well as segmentation and registration of sections.

Atlas mapping in SpinalJ is achieved by the registration of the experimental volume to the 3D Nissl template. An affine 3D transformation has to be used to prevent deformation and warping of the experimental data during registration. With this, the width-to-length ratio of the experimental dataset is fixed and must match the template. However, loss of sections can shorten the experimental data along the r-c axis (in this study, on average, 39 sections = 975 μm) and would result in mismapping. To compensate for this, SpinalJ matches the total r-c length of the experimental dataset to the length of the corresponding segment range in the template by interpolating additional sections. The current compensation approach assumes random/equal spacing of missing sections and does not account for locally concentrated losses, which can, however, be manually accommodated. With this approach, the accuracy of mapping NT signal to the GM annotation was determined to be 90% (81% for DAPI). We observed minor mismappings mainly at the transitions between wide segments of the enlargements and round segments of the thoracic SC, where slight r-c misalignment would shift GM signals into WM annotations and vice versa. Additionally, using a single Nissl reference section as a mapping template for the entire length of each segment fails to account for slight anatomical variation within segments, thus introducing mapping imprecisions. Even more accurate r-c mapping could be achieved by introducing a continuous Nissl template and allowing for the specification of additional segment key frames at multiple r-c levels in future versions of SpinalJ.

Nonetheless, with the current version of the atlas, we have demonstrated that SpinalJ can reproduce the results of various manual mapping studies. In all validation datasets, we found good agreement of SpinalJ-mapped data and known distribution patterns within GM laminae and major WM tracts of isolated spinal regions. A few minor mapping errors again typically resulted from signals shifted slightly across the original annotation outlines into neighboring annotations. For example, although AAV-labeled CST axons mapped primarily to the dcs, there was minor mismapping to the annotation of the postsynaptic dorsal column, located immediately dorsal to the dcs. For smaller annotation regions, like the individual MN clusters of lamina IX that cover only a few neurons, the mapping errors appeared larger. Mapping VAChT$^+$/Foxp1$^+$ SNs, we identified significant signal outside lamina IX, in neighboring areas laminae VII and VIII. Similarly, in samples stained for IB4$^+$ fibers, we found some mismapping to neighboring laminae outside lamina II. Improving the quality and resolution of the atlas annotations will address these minor issues of mapping imprecision. Indeed, irrespective of annotation boundaries, there was a high mapping precision of the positions of cell populations across different animals with average mapping offsets in the range of a single MN cell body diameter (13 μm for ChAT$^+$ SNs, 31 μm for VAChT$^+$/Foxp1$^+$ SNs; mapping appears slightly more precise for ChAT$^+$ SNs because centroid calculation is more robust with higher cell numbers).

Thus, with minimal inter-animal mapping offsets, SpinalJ is well suited to analyze the relative positions of known and unknown cell types and to map cells and circuits across samples, which has not been possible previously. This is illustrated by the analysis of VAChT$^+$/Foxp1$^+$ cells that revealed an unexpected population of cells in the ventral thoracic SC. Based on their position, the labeled SNs could belong to the pool of MMC or HMC MNs, although this lineage is defined by the embryonic expression of Lhx3 and the suppression of Foxp1, likely through direct co-regulation of both factors (Morikawa et al., 2009). Within the embryonic thoracic SC, Foxp1 was detected only in Isl1$^+$/pSmad$^+$ PGC neurons (Dasen et al., 2008; Morikawa et al., 2009). It is, therefore, unlikely that the labeled cells belong to MMC or HMC, unless these cells start expressing Foxp1 at later stages, something that has not been examined. Outside the population of MNs, Foxp1 expression has been observed in Pax2$^+$/En1$^+$ V1 interneurons during mid to late embryonic stages (Francius et al., 2013; Morikawa et al., 2009). These cells are positioned close to ventral MNs and generally fit the observed distribution. However, V1s have been described as inhibitory

GABAergic or glycinergic neurons, presumably excluding ChAT immunoreactivity, unless at least some V1s co-transmit acetylcholine (ACh) and GABA, as has been observed in other neurons (Lamotte d'Incamps et al., 2017; Vaaga et al., 2014). Within the group of ventral interneurons, only Pix2^{+} V0c neurons have been identified as cholinergic (Zagoraiou et al., 2009; Ziskind-Conhaim and Hochman, 2017), but Foxp1 does not co-localize with V0 markers embryonically (Morikawa et al., 2009). Further analyses and co-staining with markers for ventral interneuron classes are needed to identify the labeled cell population identified by our study.

Standardized 3D anatomical atlases, such as the ABA, generated from iterative averaging of over 1,500 different mouse brain samples (Wang et al., 2020), have proved an indispensable resource in brain research. Atlases provide a high-resolution framework for comparative analyses and have enabled massive collaborative projects like the BRAIN initiative (Ecker et al., 2017). Various computational tools have been developed for the analysis and integration of individual brain datasets (Bakker et al., 2015; Botta et al., 2020; Chon et al., 2019; Eastwood et al., 2019; Friedmann et al., 2020; Oh et al., 2014; Puchades et al., 2019; Shiffman et al., 2018; Tappan et al., 2019; Tyson et al., 2021; Wang et al., 2021), improving both speed and quality of experiments. Together, these resources have enabled brain-wide mapping studies of cell types and neuronal connectivity and dramatically accelerated scientific discovery in this field of research. In contrast, SpinalJ is the first toolbox for the 3D analysis of SC data in the context of anatomical annotations. We have demonstrated that SpinalJ provides a powerful platform for high-throughput analysis of the relative positions of populations of labeled neurons, their projection patterns, and axonal tracts. We aim to establish SpinalJ as a continuously improving resource for the field of SC research.

Limitations of study

Section registration in SpinalJ relies critically on intact spinal sections. In this study, we had to replace less than 15% of sections, distributed throughout the length of any given SC, and comparative analysis of multiple samples suggests that this intervention did not confound the real distribution of cells. However, replacing larger numbers of sections may substantially reduce axial resolution locally and introduce artifacts in cell distributions, especially when analyzing small, local cell clusters.

SpinalJ provides the first 3D atlas and a common coordinate framework for mouse SC. It should be noted, however, that the creation of this 3D atlas from 2D annotations of single sections, each from an individual segment, does not provide additional r-c resolution but instead brings the existing annotations into r-c context and into a format that allows 3D registration and atlas mapping. Importantly, the ASCA annotations are based on sections of a single animal and can therefore not account for inter-animal variability in SC anatomy. In addition, some of the smaller annotations in the ASCA (e.g., of MN clusters) appear only in one hemisegment (e.g., Ph9 in C3; Tz9, LS9, and De9 in C4; Man9 in T2). These asymmetries may have resulted from sections cut slightly obliquely or from incomplete staining but highlight the issue that the annotations for a complete segment cannot be derived reliably and with spatial precision from a single section.

To generate more stable annotations that are robust with regard to inherent anatomical variability and increase r-c resolution, additional annotation data from multiple samples are needed. However, generating additional annotation datasets involves considerable effort and time. Also, in this scenario, assignment of segment boundaries is challenging and can be achieved precisely only with the help of additional physical landmarks (e.g., nerve roots), as Nissl/AChE descriptors alone are inconclusive at some levels, especially in the thoracic SC (Harrison et al., 2013). Instead, we propose that the integration of 3D mapped populations of SNs can be used to create and improve annotations. Using cell-type-specific markers, the boundaries of anatomical landmarks and specific cell clusters will emerge in their 3D shape and can be outlined directly to refine annotations and segment boundaries after mapping to the common reference template in SpinalJ. Template mapping of registered sections relies solely on a continuous Nissl/NT reference and while, currently, the Nissl template used for mapping offers reduced detail to match the available annotations, improving template quality is easy to achieve. Providing our tools as an open resource, we hope progressively to improve the quality of the atlas with increasing numbers of datasets and markers mapped by individual laboratories and/or shared within the community. Moreover, additional 3D atlases, for example based on the annotations created for a P4 animal (Sengul et al., 2012), could be incorporated easily into SpinalJ.

STAR★METHODS

Detailed methods are provided in the online version of this paper and include the following:

- KEY RESOURCES TABLE
- RESOURCE AVAILABILITY
  - Lead contact
  - Materials availability
  - Data and code availability
- EXPERIMENTAL MODEL AND SUBJECT DETAILS
  - Animals
- METHOD DETAILS
  - 3D printing
  - Viral labeling of corticospinal neurons
  - Tissue preparation
  - Embedding
  - Sectioning and IHC
  - Imaging
  - Image processing and analysis
- QUANTIFICATION AND STATISTICAL ANALYSIS

SUPPLEMENTAL INFORMATION

Supplemental information can be found online at https://doi.org/10.1016/j.crmeth.2021.100074.

ACKNOWLEDGMENTS

We thank Samaher Fageiry for technical advice on SC tissue preparation and histology, Marcela Carmona and Anna Kim for help with cortical virus injections, Crystal K. Colón Ortiz for providing mouse eye samples, as well as

Amy Norovich and Young Mi Kwon for providing betta fish brains. We thank Susan B. Morton and the Jessell laboratory for gifts of custom antibodies. We are grateful to Carl E. Schonoover and Sarah Ohashi for help with 3D printing and thank Isobel Jessell for the term SpineRack. We thank the Mason-Dodd and Bendesky laboratories for discussion and Christoph Gebhardt for critical comments on the manuscript. Imaging was performed with support from the Zuckerman Institute's Cellular Imaging platform. This work was funded by NIH grants 1R21NS120665-01 and 5U19NS104649 and DFG grant FI 2367/1-1.

AUTHOR CONTRIBUTIONS

The study was conceptualized and directed by F.F., J.D., and C.M. F.F. developed SpineRacks and performed histology studies, imaging, and data interpretation. L.A.H. and F.F. developed SpinalJ software. D.N. provided VAChT/Foxp1 mice. F.F. and J.D. wrote the manuscript with input from all authors.

DECLARATION OF INTERESTS

Authors declare no competing interests.

Received: May 19, 2021
Revised: July 23, 2021
Accepted: August 16, 2021
Published: September 15, 2021

REFERENCES

Abraira, V.E., and Ginty, D.D. (2013). The sensory neurons of touch. Neuron *79*, 618–639.

Allen Institute for Brain Science (2008). Allen Spinal Cord Atlas. https://mousespinal.brain-map.org/imageseries/showref.html.

Bakker, R., Tiesinga, P., and Kötter, R. (2015). The scalable brain atlas: instant web-based access to public brain atlases and related content. Neuroinformatics *13*, 353–366.

Barber, R.P., Phelps, P.E., Houser, C.R., Crawford, G.D., Salvaterra, P.M., and Vaughn, J.E. (1984). The morphology and distribution of neurons containing choline acetyltransferase in the adult rat spinal cord: an immunocytochemical study. J. Comp. Neurol. *229*, 329–346.

Berg, S., Kutra, D., Kroeger, T., Straehle, C.N., Kausler, B.X., Haubold, C., Schiegg, M., Ales, J., Beier, T., Rudy, M., et al. (2019). Ilastik: interactive machine learning for (Bio)Image analysis. Nat. Methods *16*, 1226–1232.

Botta, P., Fushiki, A., Vicente, A.M., Hammond, L.A., Mosberger, A.C., Gerfen, C.R., Peterka, D., and Costa, R.M. (2020). An amygdala circuit mediates experience-dependent momentary arrests during exploration. Cell *183*, 605–619.e22.

Brown, A.G. (1982). The dorsal horn of the spinal cord. Q. J. Exp. Physiol. *67*, 193–212.

Cai, R., Pan, C., Ghasemigharagoz, A., Todorov, M.I., Förstera, B., Zhao, S., Bhatia, H.S., Parra-Damas, A., Mrowka, L., Theodorou, D., et al. (2019). Panoptic imaging of transparent mice reveals whole-body neuronal projections and skull–meninges connections. Nat. Neurosci. *22*, 317–327.

Chon, U., Vanselow, D.J., Cheng, K.C., and Kim, Y. (2019). Enhanced and unified anatomical labeling for a common mouse brain atlas. Nat. Commun. *10*, 5067.

Dasen, J.S., De Camilli, A., Wang, B., Tucker, P.W., and Jessell, T.M. (2008). Hox repertoires for motor neuron diversity and connectivity gated by a single accessory factor, Foxp1. Cell *134*, 304–316.

Delile, J., Rayon, T., Melchionda, M., Edwards, A., Briscoe, J., and Sagner, A. (2019). Single cell transcriptomics reveals spatial and temporal dynamics of gene expression in the developing mouse spinal cord. Development *146*, dev173807.

Eastwood, B.S., Hooks, B.M., Paletzki, R.F., O'Connor, N.J., Glaser, J.R., and Gerfen, C.R. (2019). Whole mouse brain reconstruction and registration to a reference atlas with standard histochemical processing of coronal sections. J. Comp. Neurol. *527*, 2170–2178.

Ecker, J.R., Geschwind, D.H., Kriegstein, A.R., Ngai, J., Osten, P., Polioudakis, D., Regev, A., Sestan, N., Wickersham, I.R., and Zeng, H. (2017). The BRAIN initiative cell census consortium: lessons learned toward generating a comprehensive brain cell atlas. Neuron *96*, 542–557.

Ertürk, A., Mauch, C.P., Hellal, F., Förstner, F., Keck, T., Becker, K., Jährling, N., Steffens, H., Richter, M., Hübener, M., et al. (2012a). Three-dimensional imaging of the unsectioned adult spinal cord to assess axon regeneration and glial responses after injury. Nat. Med. *18*, 166–171.

Ertürk, A., Becker, K., Jährling, N., Mauch, C.P., Hojer, C.D., Egen, J.G., Hellal, F., Bradke, F., Sheng, M., and Dodt, H.U. (2012b). Three-dimensional imaging of solvent-cleared organs using 3DISCO. Nat. Protoc. *7*, 1983–1995.

Francius, C., Harris, A., Rucchin, V., Hendricks, T.J., Stam, F.J., Barber, M., Kurek, D., Grosveld, F.G., Pierani, A., Goulding, M., et al. (2013). Identification of multiple subsets of ventral interneurons and differential distribution along the rostrocaudal axis of the developing spinal cord. PLoS One *8*, e70325.

Friedmann, D., Pun, A., Adams, E.L., Lui, J.H., Kebschull, J.M., Grutzner, S.M., Castagnola, C., Tessier-Lavigne, M., and Luo, L. (2020). Mapping mesoscale axonal projections in the mouse brain using a 3D convolutional network. Proc. Natl. Acad. Sci. U S A *117*, 11038–11047.

Gatto, G., Smith, K.M., Ross, S.E., and Goulding, M. (2019). Neuronal diversity in the somatosensory system: bridging the gap between cell type and function. Curr. Opin. Neurobiol. *56*, 167–174.

Goulding, M. (2009). Circuits controlling vertebrate locomotion: moving in a new direction. Nat. Rev. Neurosci. *10*, 507–518.

Häring, M., Zeisel, A., Hochgerner, H., Rinwa, P., Jakobsson, J.E.T., Lönnerberg, P., La Manno, G., Sharma, N., Borgius, L., Kiehn, O., et al. (2018). Neuronal atlas of the dorsal horn defines its architecture and links sensory input to transcriptional cell types. Nat. Neurosci. *21*, 869–880.

Harrison, M., O'Brien, A., Adams, L., Cowin, G., Ruitenberg, M.J., Sengul, G., and Watson, C. (2013). Vertebral landmarks for the identification of spinal cord segments in the mouse. Neuroimage *68*, 22–29.

Heise, C., and Kayalioglu, G. (2009). Chapter 13: Spinal Cord Transmitter Substances (Elsevier)).

Hillman, E.M.C., Voleti, V., Li, W., and Yu, H. (2019). Light-sheet microscopy in neuroscience. Annu. Rev. Neurosci. *42*, 295–313.

Hilton, B.J., Blanquie, O., Tedeschi, A., and Bradke, F. (2019). High-resolution 3D imaging and analysis of axon regeneration in unsectioned spinal cord with or without tissue clearing. Nat. Protoc. *14*, 1235–1260.

Jessell, T. (2000). Neuronal specification in the spinal cord:inductive signals and transcriptional codes. Nat. Rev. Genet. *1*, 20–29.

Johannssen, H.C., and Helmchen, F. (2013). Two-photon imaging of spinal cord cellular networks. Exp. Neurol. *242*, 18–26.

Klein, S., Staring, M., Murphy, K., Viergever, M.A., and Pluim, J.P.W. (2010). Elastix: a toolbox for intensity-based medical image registration. IEEE Trans. Med. Imaging *29*, 196–205.

Lai, H.C., Seal, R.P., and Johnson, J.E. (2016). Making sense out of spinal cord somatosensory development. Dev *143*, 3434–3448.

Lamotte d'Incamps, B., Bhumbra, G.S., Foster, J.D., Beato, M., and Ascher, P. (2017). Segregation of glutamatergic and cholinergic transmission at the mixed motoneuron Renshaw cell synapse. Sci. Rep. *7*, 1–17.

De Leener, B., Lévy, S., Dupont, S.M., Fonov, V.S., Stikov, N., Louis Collins, D., Callot, V., and Cohen-Adad, J. (2017). SCT: Spinal Cord Toolbox, an open-source software for processing spinal cord MRI data. Neuroimage *145*, 24–43.

Molliver, D.C., Radeke, M.J., Feinstein, S.C., and Snider, W.D. (1995). Presence or absence of TrkA protein distinguishes subsets of small sensory neurons with unique cytochemical characteristics and dorsal horn projections. J. Comp. Neurol. *361*, 404–416.

Morikawa, Y., Komori, T., Hisaoka, T., and Senba, E. (2009). Detailed expression pattern of foxp1 and its possible roles in neurons of the spinal cord during embryogenesis. Dev. Neurosci. *31*, 511–522.

Oh, S.W., Harris, J.A., Ng, L., Winslow, B., Cain, N., Mihalas, S., Wang, Q., Lau, C., Kuan, L., Henry, A.M., et al. (2014). A mesoscale connectome of the mouse brain. Nature *508*, 207–214.

Osseward, P.J., Amin, N.D., Moore, J.D., Temple, B.A., Barriga, B.K., Bachmann, L.C., Jr, F.B., Gullo, M., Clark, R.C., Driscoll, S.P., et al. (2021). Conserved genetic signatures parcellate cardinal spinal neuron classes into local and projection subsets. Science *393*, 385–393.

Pan, C., Cai, R., Quacquarelli, F.P., Ghasemigharagoz, A., Lourbopoulos, A., Matryba, P., Plesnila, N., Dichgans, M., Hellal, F., and Ertürk, A. (2016). Shrinkage-mediated imaging of entire organs and organisms using uDISCO. Nat. Methods *13*, 859–867.

Prados, F., Cardoso, M.J., Yiannakas, M.C., Hoy, L.R., Tebaldi, E., Kearney, H., Liechti, M.D., Miller, D.H., Ciccarelli, O., Wheeler-Kingshott, C.A.M.G., et al. (2016). Fully automated grey and white matter spinal cord segmentation. Sci. Rep. *6*, 1–10.

Prasad, A., and Hollyday, M. (1991). Development and migration of avian sympathetic preganglionic neurons. J. Comp. Neurol. *307*, 237–258.

Pratt, V. (1987). Direct least-squares fitting of algebraic surfaces. Comput. Graph. *21*, 145–152.

Puchades, M.A., Csucs, G., Ledergerber, D., Leergaard, T.B., and Bjaalie, J.G. (2019). Spatial registration of serial microscopic brain images to three-dimensional reference atlases with the QuickNII tool. PLoS One *14*, 1–14.

Qi, Y., Yu, T., Xu, J., Wan, P., Ma, Y., Zhu, J., Li, Y., Gong, H., Luo, Q., and Zhu, D. (2019). FDISCO: advanced solvent-based clearing method for imaging whole organs. Arch. Di Stud. Urbani e Reg. *48*, 1–14.

Quinn, B., Toga, A.W., Motamed, S., and Merlic, C.A. (1995). Fluoro Nissl Green: a novel fluorescent counterstain for neuroanatomy. Neurosci. Lett. *184*, 169–172.

Renier, N., Wu, Z., Simon, D.J., Yang, J., Ariel, P., and Tessier-Lavigne, M. (2014). IDISCO: a simple, rapid method to immunolabel large tissue samples for volume imaging. Cell *159*, 896–910.

Rexed, B. (1954). A cytoarchitectonic atlas of the spinal cord in the cat. J. Comp. Neurol. *100*, 297–379.

Rosenberg, A.B., Roco, C.M., Muscat, R.A., Kuchina, A., Sample, P., Yao, Z., Graybuck, L.T., Peeler, D.J., Mukherjee, S., Chen, W., et al. (2018). Single-cell profiling of the developing mouse brain and spinal cord with split-pool barcoding. Science *360*, 176–182.

Sathyamurthy, A., Johnson, K.R., Matson, K.J.E., Dobrott, C.I., Li, L., Ryba, A.R., Bergman, T.B., Kelly, M.C., Kelley, M.W., and Levine, A.J. (2018). Massively parallel single nucleus transcriptional profiling defines spinal cord neurons and their activity during behavior. Cell Rep. *22*, 2216–2225.

Schindelin, J., Arganda-Carreras, I., Frise, E., Kaynig, V., Longair, M., Pietzsch, T., Preibisch, S., Rueden, C., Saalfeld, S., Schmid, B., et al. (2012). Fiji: an open-source platform for biological-image analysis. Nat. Methods *9*, 676–682.

Schmid, B., Schindelin, J., Cardona, A., Longair, M., and Heisenberg, M. (2010). A high-level 3D visualization API for Java and ImageJ. BMC Bioinformatics *11*, 274.

Sengul, G., Puchalski, R.B., and Watson, C. (2012). Cytoarchitecture of the spinal cord of the postnatal (p4) mouse. Anat. Rec. *295*, 837–845.

Sherrington, C.S. (1906). The Integrative Action of the Nervous System (C. Scribner and Sons).

Shiffman, S., Basak, S., Kozlowski, C., and Fuji, R.N. (2018). An automated mapping method for Nissl-stained mouse brain histologic sections. J. Neurosci. Methods *308*, 219–227.

Silverman, J.D., and Kruger, L. (1990). Selective neuronal glycoconjugate expression in sensory and autonomic ganglia: relation of lectin reactivity to peptide and enzyme markers. J. Neurocytol. *19*, 789–801.

Soderblom, C., Lee, D.H., Dawood, A., Carballosa, M., Santamaria, A.J., Benavides, F.D., Jergova, S., Grumbles, R.M., Thomas, C.K., Park, K.K., et al. (2015). 3D imaging of axons in transparent spinal cords from rodents and nonhuman primates. ENeuro *2*, 1–23.

Stachowski, N.J., and Dougherty, K.J. (2021). Review spinal inhibitory interneurons: gatekeepers of sensorimotor pathways. Int. J. Mol. Sci. *22*, 1–17.

Stifani, N. (2014). Motor neurons and the generation of spinal motor neuron diversity. Front. Cell. Neurosci. *8*, 1–22.

Takazawa, T., Choudhury, P., Tong, C.K., Conway, C.M., Scherrer, G., Flood, P.D., Mukai, J., and Macdermott, A.B. (2017). Inhibition mediated by glycinergic and GABAergic receptors on excitatory neurons in mouse superficial dorsal horn is location-specific but modified by inflammation. J. Neurosci. *37*, 2336–2348.

Tappan, S.J., Eastwood, B.S., O'Connor, N., Wang, Q., Ng, L., Feng, D., Hooks, B.M., Gerfen, C.R., Hof, P.R., Schmitz, C., et al. (2019). Automatic navigation system for the mouse brain. J. Comp. Neurol. *527*, 2200–2211.

Thévenaz, P., Ruttimann, U.E., and Unser, M. (1998). A pyramid approach to subpixel registration based on intensity. IEEE Trans. Image Process. *7*, 27–41.

Tian, T., and Li, X. (2020). Applications of tissue clearing in the spinal cord. Eur. J. Neurosci. *52*, 4019–4036.

Tripodi, M., Stepien, A.E., and Arber, S. (2011). Motor antagonism exposed by spatial segregation and timing of neurogenesis. Nature *479*, 61–66.

Tsuchida, T., Ensini, M., Morton, S.B., Baldassare, M., Edlund, T., Jessell, T.M., and Pfaff, S.L. (1994). Topographic organization of embryonic motor neurons defined by expression of LIM homeobox genes. Cell *79*, 957–970.

Tyson, A.L., Rousseau, C.V., Niedworok, C.J., Keshavarzi, S., Tsitoura, C., and Margrie, T.W. (2021). A deep learning algorithm for 3D cell detection in whole mouse brain image datasets. PLoS Comput. Biol. *17*, e1009074.

Ueda, H.R., Ertürk, A., Chung, K., Gradinaru, V., Chédotal, A., Tomancak, P., and Keller, P.J. (2020). Tissue clearing and its applications in neuroscience. Nat. Rev. Neurosci. *21*, 61–79.

Ueno, M., Nakamura, Y., Li, J., Gu, Z., Niehaus, J., Maezawa, M., Crone, S.A., Goulding, M., Baccei, M.L., and Yoshida, Y. (2018). Corticospinal circuits from the sensory and motor cortices differentially regulate skilled movements through distinct spinal interneurons. Cell Rep *23*, 1286–1300.e7.

Vaaga, C.E., Borisovska, M., and Westbrook, G.L. (2014). Dual-transmitter neurons: functional implications of co-release and co-transmission. Curr. Opin. Neurobiol. *29*, 25–32.

Vigouroux, R.J., Belle, M., and Chédotal, A. (2017). Neuroscience in the third dimension: shedding new light on the brain with tissue clearing. Mol. Brain *10*, 1–10.

Wang, Q., Ding, S.L., Li, Y., Royall, J., Feng, D., Lesnar, P., Graddis, N., Naeemi, M., Facer, B., Ho, A., et al. (2020). The Allen mouse brain common coordinate framework: a 3D reference atlas. Cell *181*, 936–953.e20.

Wang, X., Zeng, W., Yang, X., Fang, C., Han, Y., and Fei, P. (2021). Bi-channel image registration and deep-learning segmentation (Birds) for efficient, versatile 3D mapping of mouse brain. eLife *10*, 1–20.

Zagoraiou, L., Akay, T., Martin, J.F., Brownstone, R.M., Jessell, T.M., and Miles, G.B. (2009). A cluster of cholinergic premotor interneurons modulates mouse locomotor activity. Neuron *64*, 645–662.

Zhao, S., Todorov, M.I., Cai, R., Maskari, R.A., Steinke, H., Kemter, E., Mai, H., Rong, Z., Warmer, M., Stanic, K., et al. (2020). Cellular and molecular probing of intact human organs. Cell *180*, 796–812.e19.

Ziskind-Conhaim, L., and Hochman, S. (2017). Diversity of molecularly defined spinal interneurons engaged in mammalian locomotor pattern generation. J. Neurophysiol. *118*, 2956–2974.

STAR★METHODS

KEY RESOURCES TABLE

REAGENT or RESOURCE	SOURCE	IDENTIFIER
Antibodies		
Rabbit polyclonal anti-RFP	Rockland Immunochemicals	Cat#600-401-379; RRID: AB_2209751
Guinea pig polyclonal anti-dsRed	Gift of Jessell lab	N/A
Goat polyclonal anti-ChAT	Millipore Sigma	Cat#AB144P; RRID: AB_2079751
Bacterial and virus strains		
AAV2.1-CAG-tdTomato	UNC vector core	Lot#AV6325C
Chemicals, peptides, and recombinant proteins		
Isolectin B4, FITC-conjugated	Sigma-Aldrich	Cat#L2895
Neurotrace 500/525	Thermo Fisher Scientific	Cat#N21480
Neurotrace 640/660	Thermo Fisher Scientific	Cat#N21483
DAPI	Thermo Fisher Scientific	Cat#D1306
Deposited data		
SpineRack and SpinalJ user guide	This study	Zenodo: https://doi.org/10.5281/zenodo.5177185; https://github.com/felixfiederling/SpinalJ
3D SC reference atlas p56	This study	Zenodo: https://doi.org/10.5281/zenodo.5177185
Raw data and analysis spreadsheets	This study	Mendeley Data: https://doi.org/10.17632/6hf6tt3xwj.1
Software and algorithms		
Fiji (ImageJ)	NIH	https://fiji.sc/
SpinalJ	This study	Zenodo: https://doi.org/10.5281/zenodo.5177185
Ilastik 1.3.3	Berg et al., 2019	https://www.ilastik.org/
Matlab	Mathworks	https://www.mathworks.com/products/matlab.html
NIS-Elements JOBS	Nikon Instruments	https://www.microscope.healthcare.nikon.com/en_EU/products/software/nis-elements/nis-elements-jobs
JOBS settings for imaging	This study	Zenodo: https://doi.org/10.5281/zenodo.5177185
Other		
PVA filament	Ultimaker	Cat#9731
SpineRack .stl print file	This study	Zenodo: https://doi.org/10.5281/zenodo.5177185

RESOURCE AVAILABILITY

Lead contact

Further information and requests for resources and reagents should be directed to and will be fulfilled by the lead contact, Jane Dodd (jd18@columbia.edu).

Materials availability

This study did not generate new unique reagents.

Data and code availability

- Processed data have been deposited at Github and are publicly available as of the date of publication. DOIs are listed in the key resources table. Microscopy data reported in this paper will be shared by the lead contact upon request.
- All original code has been deposited at Github and is publicly available as of the date of publication. DOIs are listed in the key resources table.
- Any additional information required to reanalyze the data reported in this paper is available from the lead contact upon request.

EXPERIMENTAL MODEL AND SUBJECT DETAILS

Animals

All experimental protocols were approved by the Columbia University Institutional Animal Care and Use Committee. All experimental animals were adult (>3 month old) male and female mice housed on a 12h light/dark cycle with *ad libitum* access to food and water. Unless stated otherwise, we used C57BL/6J animals for tool development and validation. To label cholinergic, Foxp1 expressing neurons, we used *FoxP1::FonCre*$^{FonCre/+}$; *VAChT::FlpO*$^{FlpO/+}$; *Ai9*$^{Ai9/+}$ mice. In *FoxP1::FonCre*$^{FonCre/+}$ mice, Cre recombinase is incorporated at the 3' end of *FoxP1* using a P2A linker to avoid disruption of *FoxP1* expression. The Cre open-reading-frame is interrupted by a 'stop cassette' flanked by F3 FRT sequences, and is restored with Flp expression. Both *FoxP1::FonCre*$^{FonCre/+}$ and *VAChT::FlpO*$^{FlpO/+}$ mice were generated by homologous recombination using mouse ES cells. The details of these two mouse lines will be presented elsewhere (D.N., unpublished data).

METHOD DETAILS

3D printing

SpineRack embedding scaffolds were designed using Autodesk TinkerCAD (https://www.tinkercad.com/; Autodesk) and printed from Ultimaker Polyvinyl alcohol (PVA) filament (Ultimaker B.V.) on a dual extruder Ultimaker 3 printer. Ultimaker Cura software was used for slicing and printer setup (material: natural PVA; print core: BB 0.4; layer height: 0.15mm; print temp: 220°C, bed: 60°C; infill: 20%; build plate adhesion: brim 3mm).

For all results shown, we used SpineRacks with outer dimensions: 11mm x 11mm x 4.0mm, well size: 3.0mm x 3.0mm x 4.0mm, wall thickness: 0.5mm. Other dimensions are easily achieved. Print files are available for download (see key resources table).

PVA is hygroscopic and to prevent absorbance of moisture from room air filament and printed racks should be stored in the dark in an air tight container along with a desiccant. Under these conditions, we have found that SpineRacks can be stored for at least one year without qualitative changes, swelling or shrinking.

Viral labeling of corticospinal neurons

Cortical virus injections were performed under sterile conditions and isoflurane anesthesia (1–3%, plus oxygen at 1-1.5L/min) on a stereotactic frame (David Kopf Instruments, Model 900SD). Throughout surgery, mouse body temperature was maintained at 37°C using an animal temperature controller (FHC, Model 40-90-8D) and, afterward, mice were allowed to recover from the anesthesia in their homecage on a heating pad. Before surgery, animals were subcutaneously injected with Buprenorphine SR (0.5-1mg/kg). The mouse head was shaved, cleaned with 70% alcohol and iodine, an intradermic injection of bupivacaine was administered and the skull was exposed to permit alignment of the head and drilling of the hole for the injection site. 500nl of AAV2.1-CAG-TdTomato (titer: $5.3x10^{12}$ vg/ml; UNC, lot AV6325C) was injected across five injection sites into the left hemisphere of the motor and sensory cortex (central coordinate: AP -.25mm, ML 1.5mm, and DV between .45-.85mm with four additional injections spaced ~500μm apart, forming a square around the center) using a Nanojet III Injector (Drummond Scientific, USA) at a pulse rate of 1nl/s, injecting 20-25nl every 100–200μm. The injection pipette was left in place for 10min post-injection before it was slowly removed (rate 200μm/s). After injections, the small whole made during the craniotomy was filled with kwik-sil silicon adhesive (World Precision Instruments, USA) and the skin was closed using sutures. After 4 weeks, mice were euthanized and perfused as described below. Brains were embedded in 2% agarose and sectioned on a vibratome at 100μm. To determine the position and extent of injection sites, images of brain sections were registered and mapped to the Allen Mouse Brain Atlas using BrainJ, as described in Botta et al. (2020).

Tissue preparation

Mice were perfused with 4% paraformaldehyde (PFA) in PBS and the spinal column was post-fixed in 4% PFA overnight at 4°C after exposing the SC through ventral laminectomy. The SC was then isolated, washed 3x in cold PBS and cryo-protected in 30% sucrose solution at 4°C until the tissue had sunk.

To optimize sectioning efficiency of the whole SC, nine sequential tissue pieces were mounted in one block. For this, the SC was first trimmed caudally, removing segments caudal to S1 and the *cauda equina*. We then split the remaining cord, spanning all cervical, thoracic and lumbar segments, into three equal sized tissue pieces using iridectomy scissors. Each of these pieces was then split again into three equal sized pieces, resulting in a total of nine, 3-4mm long tissue pieces (Figures 1A–1D; for detailed instructions, see user guide, link in key resources table).

Embedding

For embedding, a truncated 12mm plastic mold (Peel-A-Way T12; Polysciences) was filled with Tissue-Tek OCT Compound (Sakura Finetek USA). A SpineRack was then sunk into the OCT and pushed to the bottom of the mold using blunt forceps. Air bubbles trapped in the structure were removed using the sharp points of forceps. Spinal tissue pieces were gently placed into each well, until the rostral cut face touched the bottom of the mold. Pieces 1 to 3 were embedded (left to right) in the top row, pieces 4 to 6 in the middle row and pieces 7 to 9 in the bottom row of the rack (Figures 1E–1I). Other tissues (fish brains, mouse eyes) were embedded similarly. To facilitate easy cryo-sectioning through the block containing SpineRack and tissue pieces, the filled mold was left at

room temperature for 20–25min before freezing. This allowed the SpineRacks partially to dissolve and soften in the OCT and to achieve consistent texture across the block. Filled molds were then frozen on dry ice in a slush of absolute ethanol and crushed dry ice and resultant blocks stored at −80°C until use.

Sectioning and IHC

Blocks were sectioned on a Leica CM3050S cryostat (Leica Biosystems) at 25μm. Sections were collected on Fisherbrand Superfrost Plus slides (Fisher Scientific). Eight consecutive sections were collected in two rows on each slide (Figures 1J and 1K). Slides were washed in Wheaton staining dishes filled with PBS, for 5 min on an orbital shaker, to dissolve OCT and SpineRack material. Sections were incubated with primary antibodies in PBS containing 0.1% Triton X-100 at 4°C overnight, then washed in PBS and incubated with secondary antibodies, DAPI and/or Neurotrace in PBS for 1-2h at room temperature. tdTomato signal was amplified using anti RFP or anti dsRed antibodies. See key resources table for material details.

Imaging

Slides were imaged using a motorized Nikon AZ100 Multizoom microscope (Nikon Instruments) equipped with an automated slide feeder (Prior Scientific) and Andor Zyla sCMOS camera (Oxford Instruments). Images were acquired using a Nikon 4x 0.4 NA AZ Plan Apo objective with an additional 2.1× magnification, resulting in an image pixel size of 1μm/pixel. Each block section (3x3 array of nine tissue sections) was scanned and saved as one image file (.nd2 format, containing stage coordinate metadata) using NIS-Elements JOBS software (configuration file available for download at; see key resources table). To do this, the software was programmed to scan the entire slide at low resolution in a single channel (DAPI or NT). A manually determined threshold was then applied automatically to isolate tissue sections from background and a dilation factor was used to add pixels to the object boundaries and merge all tissue sections of a block section into a single object. The identified block section objects were then scanned in all channels. This approach allowed us to keep the positional information of tissue sections within a block section, which is essential to identify individual tissue sections, while keeping the file size of images in a manageable range (1-2GB per block section image). We imaged a single optical plane of each 25μm section, assuming that there would be minimal overlap of cell somata in the z direction with spinal cell types ranging from 7–45μm in diameter (Sengul et al., 2012).

Image processing and analysis

Images of SC tissue sections were processed and reconstructed in Fiji/ImageJ (Schindelin et al., 2012) using SpinalJ, a plugin developed in this study combining software tools to facilitate image registration, atlas mapping and 3D analysis of SC sections. SpinalJ and a detailed, step-by-step user guide are freely available for download (see key resources table).

For easy visualization of data, SpinalJ creates plots of absolute and relative signal intensities, cell densities and projection densities as heatmap montages for each spinal segment. In addition, we used the 3D viewer plugin for Fiji (Schmid et al., 2010) to render 3D views of reconstructed datasets. 2D/3D cell position plots were created in MATLAB (Mathworks) using the '*scatter*' and '*scatter3'* functions, respectively. Similarly, heatmap chart matrix plots were created in MATLAB using the '*heatmap*' function.

All image processing and analysis was performed on a workstation running Windows 10 Enterprise 64 bit, equipped with a 16 core Intel i9 7960 × 2.8GHz CPU, 128 GB DDR4 memory, a 1TB Samsung 860 SSD and a 12GB Nvidia Titan X video card. SpinalJ processing generates a significant amount of data per dataset (2–3 fold original data) to allow for validation of results and reprocessing when required, but these intermediate data can be deleted following successful processing.

QUANTIFICATION AND STATISTICAL ANALYSIS

All values are shown as mean ± standard deviation (SD). Statistical details of experiments are provided in figure legends.